Inverse Acoustic Methodology for Continuous Scan Phased Arrays

Dimitri Papamoschou * and David Morata †
University of California, Irvine, CA, 92697-3975, USA

Parthiv Shah‡
ATA Engineering, San Diego, CA, 92128, USA

The paper presents a methodology for the direct estimation of the spatio-spectral distribution of an acoustic source from microphone measurements that comprise fixed and continuously scanning sensors. The non-stationarity introduced by the sensor motion is quantified by means of the Wigner-Ville spectrum. Its strongest effect is on the correlations of the sensor signals. Suppression of the non-stationarity in the signal processing involves division of the signals into blocks and application of a frequency-dependent window within each block. The direct estimation approach entails the inversion of an integral that connects the source distribution to the measured coherence of the acoustic field. A Bayesian-estimation approach is developed that allows for efficient inversion of the integral and performs similarly to the much costlier conjugate gradient method. The methodology is applied to acoustic fields emitted by impinging jets approximating a point source and an overexpanded supersonic jet. The measurement setup comprises one continuously scanning microphone and a number of fixed microphones, all arranged on a linear array. Comparisons are made between array configurations with fixed microphones only and with the scanning microphone, all having the same sensor count. The noise source maps with the scanning microphone have improved spatial fidelity and suppressed sidelobes. The ability of the continuous scan paradigm to provide high-definition noise source maps with low sensor count is demonstrated.

Nomenclature

a	=	speed of sound
c	=	coefficient
D	=	jet diameter
f	=	cyclic frequency
g	=	frequency-dependent window

*Professor, Department of Mechanical and Aerospace Engineering, Fellow AIAA.
†Graduate Student Researcher, Department of Mechanical and Aerospace Engineering, Student Member AIAA.
‡Senior Technical Advisor, Senior Member AIAA.

G	=	cross-spectral matrix
J	=	number of distinct elements of coherence matrices
K	=	number of blocks
ℓ	=	source-sensor distance
M	=	number of microphones
N	=	length of frequency vector
N_{FFT}	=	size of Fast Fourier Transform
r	=	radial distance
p	=	pressure fluctuation
S	=	number of segments in a block
Sr	=	Strouhal number = fD/U
t	=	time
T	=	block duration
U	=	fully-expanded jet velocity
V	=	sensor speed
x	=	axial coordinate
y	=	transverse coordinate
Z	=	array response matrix
α	=	derivative given by Eq. 6
β	=	Doppler factor (Eq. 9)
δ	=	width of Gaussian window
θ	=	polar angle relative to jet axis
Θ	=	directivity matrix
λ	=	acoustic wavelength
ξ	=	axial coordinate; virtual coordinate in Bayesian estimation
ψ	=	coherence-based source distribution
Ψ	=	spectrum-based source distribution
τ	=	source-sensor time; time separation in correlations
ω	=	angular frequency
ω'	=	Doppler-shifted frequency (Eq. 16)
ω''	=	frequency of spectral oscillation (Eq. 17)

Subscripts

f	=	fixed sensor
k	=	block index
m	=	microphone index
n	=	microphone index; frequency index
s	=	segment index; scanning sensor

Acronyms

FFT	=	Fast Fourier Transform
SPL	=	sound pressure level
WVS	=	Wigner-Ville spectrum
XWVS	=	cross Wigner-Ville spectrum

I. Introduction

In the field of imaging of aeroacoustic sources, there is increasing interest in methods wherein the entirety or a subset of the sensors traverse prescribed paths in a continuous motion. The continuous-scan approach can be considered as an extension of the stop-and-start (fixed indexing) method of Ref. Lee and Bolton [1] and has found applications in near-field holography [2, 3], order tracking [4] and beamforming [5]. Analogous beamforming problems involve the imaging of moving sources using fixed sensors [6]. Continuous scan can provide very high spatial resolution and reduction in the sensor count. Order-of-magnitude reduction in acquisition time, with same measurement quality, has been achieved in comparison to fixed-position sensors [7] or fixed indexing [8]. Further, continuous scan can prevent damage to the sensors by the impulsive accelerations associated with fixed indexing. Challenges include the treatment of non-stationary signals due to the motion of the sensors.

Traditional beamforming generates noise source images by “steering" the sensors to the region of interest, using techniques such as the delay-and-sum method [9, 10]. The resulting image is a convolution between the modeled source distribution (e.g., a distribution of uncorrelated monopoles) and the array point spread function. To improve the spatial resolution of the image, and reject the sidelobes that are inherent in the point spread function, various deconvolution approaches have been developed [11–14]. On the other hand, the entire steering approach can be obviated by estimating the source distribution directly via least-squares minimization of the difference between the modeled and measured pressure statistics [15]. These statistics are typically in the forms of the cross-spectral or coherence matrices. The resulting direct spectral estimation method, applied to the coherence field, has been shown to provide results comparable to the deconvolution in the imaging of sound from turbulent jets and allows for the self-consistent treatment of directional sources [14]. The direct approach allows for the treatment of advanced models for the noise sources [16], even though the present study is confined to the traditional treatment of uncorrelated monopoles.

The main interest here is the application of the coherence-based, direct spectral estimation method to the continuous-scan paradigm. An analytical development provides an approximation to the far-field coherence, as measured by fixed and scanning sensors (sensors that move during the data acqusition), and quantifies the effects of non-stationarity. Filtering methods are then proposed to mitigate the effects of non-stationarity on the measured acoustic field. The inversion of the resulting acoustic problem, wherein the source statistics are inferred directly from the measured coherence field, is addressed via the conjugate gradient method and a novel implementation of Bayesian estimation. The methodology is applied to experiments that use a fluidic "point source" and a supersonic jet. The study is complementary to ongoing efforts on multi-reference continuous scan methods using similar sources [17].

II. Model for the Acoustic Field

A. Preliminary Concepts

The primary challenge in processing acoustic data from moving sensors involves the treatment of signals that are not stationary in time. Before developing such a theoretical treatment, it is useful to think broadly about the sources of non-stationarity and develop dimensionless parameters that could characterize them. Consider a source fixed in space and emitting a signal that is stationary in time; and a sensor moving with speed V for duration T in the acoustic field emitted by this source. The emitted acoustic field has spatial variations in its statistics, that is, it is non-stationary in space. The first cause of (temporal) non-stationarity is the traversing of the sensor through an acoustic field with spatially-varying statistics. Assuming that the spatial variation has length scale X, non-stationarity scales with VT/X. The sensor signal is also affected by a Doppler shift that depends on the Mach number of the sensor, V/a, and its trajectory relative to the source. So, a second source of non-stationarity is the variation of the Doppler shift with sensor position; this will depend on the specifics of the trajectory, but in a general sense is governed by V/a.

Suppose now that we correlate the signals of two sensors, one fixed and the other moving with speed V relative to the fixed sensor and in the direction of propagation of the acoustic field. The signal of the moving sensor will be subject to the aforementioned two sources of non-stationarity. However, the correlation between the fixed and the scanning sensors will also be affected by the displacement of the moving sensor in relation to the acoustic wavelength, that is, VT/λ. This third source of non-stationarity can be quite severe at high frequency (small wavelength).

The above arguments can be easily extended to arbitrary motions of a pair of sensors; nevertheless, the simple situations above help identify the dimensionless groupings VT/X, V/a, and VT/λ as broad measures of non-stationarity. They will emerge, in refined forms, in the development of the theoretical model presented next. At this point, the insight we get is that all these dimensionless parameters will need to be small to treat the signals as quasi-stationary.

Clearly a slow scan is beneficial in this regard, but there are bounds as to how small V can be without resulting in excessive storage and processing requirements, and possibly in increased experimental costs.

B. Wigner-Ville Spectrum

Among several techniques proposed for the processing of non-stationary random variables, the Wigner-Ville spectrum (WVS) has gained prominence (Martin and Flandrin [18]). Considering a non-stationary random signal $u(t)$, its *symmetric* autocorrelation is

$$R_{uu}(t,\tau) \;=\; \left\langle u\left(t+\frac{\tau}{2}\right)\; u^*\left(t-\frac{\tau}{2}\right)\right\rangle \tag{1}$$

where $< >$ denotes the expected value (ensemble average) and $(\,)^*$ is the complex conjugate. The WVS is defined as the Fourier transform of the symmetric autocorrelation,

$$G_{uu}(t,\omega) \;=\; \int_{-\infty}^{\infty} R_{uu}(t,\tau)e^{-i\omega\tau}d\tau \tag{2}$$

Similarly, for two random variables $u(t)$ and $v(t)$, the cross Wigner-Ville spectrum(XWVS) [19] is

$$G_{uv}(t,\omega) \;=\; \int_{-\infty}^{\infty} R_{uv}(t,\tau)e^{-i\omega\tau}d\tau \tag{3}$$

The above expressions reduce to the common expressions for the auto- and cross-spectral densities for stationary processes when $R_{uu}(t,\tau) = R_{uu}(\tau)$ and $R_{uv}(t,\tau) = R_{uv}(\tau)$.

A practical limitation in the application of the WVS or XWVS is the lack of ensemble averages to form the correlations R_{uu} and R_{uv} [18]. For stationary processes, the principle of ergodicity is used to replace the ensemble average with the time average. This is not possible for a non-stationary signal, unless the time averaging is confined to an interval over which the signal can be considered quasi-stationary. Criteria for quasi-stationarity in terms of the correlation have been proposed in Refs. [18] and [19]. Here, the time dependence of the XWVS will be derived explicitly and criteria for its suppression will be formulated accordingly. Regardless of the method used, the outcome is that the signal needs to be segmented into appropriately-sized blocks and the cross-spectral analysis is done within each block. Although the focus of this study is on moving sensors, the generic methodology developed will be adaptable to moving sources as well.

C. Line Source Model for the Jet Noise Source

Consider the line source model of Fig. 1, where ξ is the source coordinate. We allow for directional sources and denote the source distribution $q(\xi,\theta,t)$, with θ the polar angle measured from location ξ. A series of M microphone sensors is deployed, each sensor traversing with a speed V_m along a path parallel to the source line. Assuming spherical spreading in a quiescent medium with uniform speed of sound a, and allowing for slow scan with $V_m << a$, the pressure recorded by sensor m is [5]

$$p_m(t) = \int_{\mathcal{L}} \frac{1}{\ell_m(\xi,t)} q\left[\xi,\ \theta_m(\xi,t),\ t - \tau_m(\xi,t)\right] d\xi \tag{4}$$

where

$$\tau_m(\xi,t) = \frac{\ell_m(\xi,t)}{a} \tag{5}$$

is the source-sensor propagation time. Integration is carried over the region of interest $\mathcal{L}$ where significant sound sources are expected.

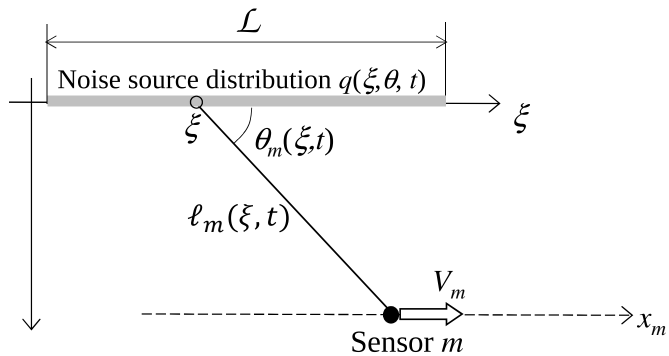

Fig. 1 Line source model.

D. Segmentation into Blocks

The sensor signal $p_m(t)$ is non-stationary because of the time-varying distance $\ell_m(\xi,t)$ and polar angle $\theta_m(\xi,t)$. This represents the first source of non-stationarity discussed in Section II.A. Quasi-stationarity is sought by segmenting the signal into blocks, as illustrated in Fig. 2. The blocks can be overlapping or non-overlapping. Considering block k with center time t_k and duration T, subscript mk denotes the quantities associated with sensor m at $t = t_k$. The following approximations are made:

$$\begin{aligned}
\tau_m(\xi,t) &\approx \tau_{mk}(\xi) + \alpha_{mk}(\xi)(t - t_k)\ ,\ \alpha_{mk}(\xi) = \left(\frac{\partial \tau_m(\xi,t)}{\partial t}\right)_{t=t_k} \\
\ell_m(\xi,t) &\approx \ell_{mk}(\xi) \\
\theta_m(\xi,t) &\approx \theta_{mk}(\xi)
\end{aligned} \tag{6}$$

Recalling the discussion of Section II.A, these approximations reflect the constraint $V_m X/T << 1$, where X is a characteristic length of the spatial variation of the variance of $p_m(t)$. For an omnidirectional source, and for the linear sensor path depicted in Fig. 1, it would be reasonable to set $X = \ell_m$. For a source with directional emission, X would need to be carefully selected based on the sharpest spatial gradient along the trajectory of the sensor. The first line in

Eq. 6 is the Taylor expansion of τ_m around $t = t_k$. The linear term is retained because it can cause a non-trivial time lag. The distance (spherical spreading) and polar angle do not cause time lags and, consistent with the above constraint, are treated as constant within a given block. It is easy to show that

$$\alpha_{mk}(\xi) \;=\; \frac{V_m}{a}\,\frac{x_{mk}-\xi}{\ell_{mk}(\xi)} \;=\; \frac{V_m}{a}\cos\theta_{mk}(\xi) \tag{7}$$

For slow scan speed, α_{mk} is a very small number. However, at high frequency it can introduce significant phase changes that cannot be neglected. Understanding that all the geometric and source variables with subscript mk depend on the source coordinate ξ, the argument ξ is henceforth omitted for brevity. Written for block k, Eq. 4 takes the form

$$p_{mk}(t) \;=\; \int_{\mathcal{L}} \frac{1}{\ell_{mk}} q\big(\xi,\ \theta_{mk},\ \beta_{mk} t - \tau_{mk}\big)\, d\xi \tag{8}$$

where

$$\beta_{mk} = 1 - \alpha_{mk} \;=\; 1 - \frac{V_m}{a}\cos\theta_{mk}(\xi) \tag{9}$$

can be thought of as a Doppler factor that stretches or compresses the time t.

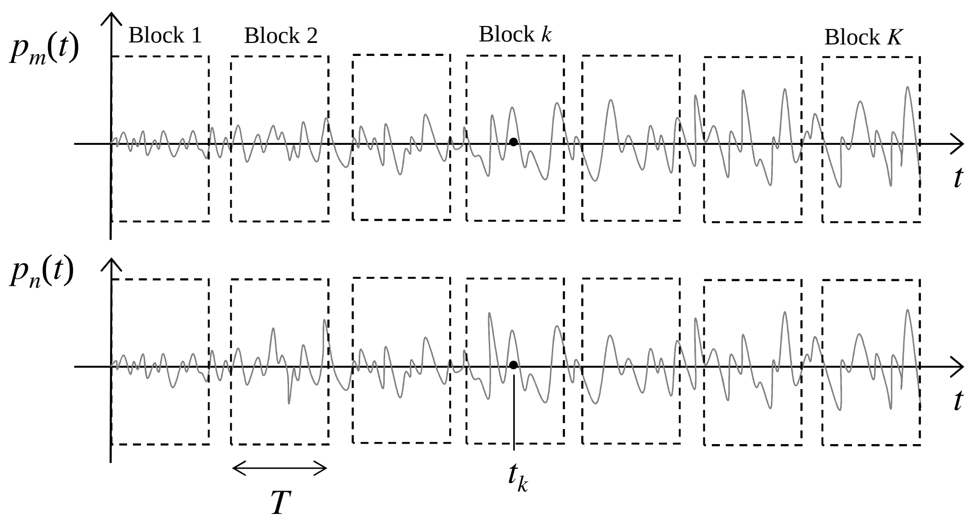

Fig. 2 Segmentation of the non-stationary signals of sensors m and n into K quasi-stationary blocks.

E. Cross Correlations

The sensor signals are cross-correlated for each block. It is convenient to reference the time coordinate to the center time t_k. The symmetric cross-correlation of signals $p_{mk}(t)$ and $p_{nk}(t)$ is

$$\begin{aligned} &\left\langle p_{mk}\left(t+\frac{\tau}{2}\right) p^*_{nk}\left(t-\frac{\tau}{2}\right)\right\rangle \;=\; \\ &\int_{\mathcal{L}}\int_{\mathcal{L}} \frac{1}{\ell_{mk}\ell_{nk}} \left\langle q(\xi,\theta_{mk},\beta_{mk}(t+\tau/2)-\tau_{mk})\; q^*(x,\theta_{nk},\beta_{nk}(t-\tau/2)-\tau_{nk})\right\rangle dx d\xi \end{aligned} \tag{10}$$

where Eq. 8 was used to connect it to the cross-spectral density of the source. In Eq. 10, the left hand side is dependent on τ and weakly dependent on t (quasi-stationarity), whereas q is stationary and thus $< qq^* >$ depends only on the time separation. On defining $t' = \beta_{nk}(t-\tau/2)-\tau_{nk}$, Eq. 10 is re-written as

$$\left\langle p_{mk}\left(t+\frac{\tau}{2}\right) p^*_{nk}\left(t-\frac{\tau}{2}\right)\right\rangle \;=\; \int_{\mathcal{L}}\int_{\mathcal{L}} \frac{1}{\ell_{mk}\ell_{nk}} \left\langle q(\xi,\theta_{mk},t'+\tau')\; q^*(x,\theta_{nk},t')\right\rangle dx d\xi \tag{11}$$

with

$$\tau' \;=\; t(\beta_{mk}-\beta_{nk}) + \frac{\tau}{2}(\beta_{mk}+\beta_{nk}) + \tau_{nk} - \tau_{mk} \tag{12}$$

The first term on the right-hand side of Eq. 12 indicates a time separation τ' that stretches or contracts with time t. This is the principal source of non-stationarity of the sensor correlation.

F. Cross-Spectral Densities

Using Eq. 3, the XWVS of the sensor signals in block k is

$$G_{mnk}(t,\omega) \;=\; \int_{-\infty}^{\infty} \left\langle p_{mk}\left(t+\frac{\tau}{2}\right) p^*_{nk}\left(t-\frac{\tau}{2}\right)\right\rangle e^{-i\omega\tau}\; d\tau \tag{13}$$

Inserting Eqs. 11 and 12, and defining the cross-spectral density of the source as

$$Q_{mnk}(x,\xi,\omega) \;=\; \int_{-\infty}^{\infty} \left\langle q(\xi,\theta_{mk},t+\tau) q^*(x,\theta_{nk},t)\right\rangle e^{-i\omega\tau}\; d\tau, \tag{14}$$

the XWVS becomes

$$\begin{aligned} G_{mnk}(t,\omega) \;=\; &\int_{\mathcal{L}}\int_{\mathcal{L}} \frac{2Q_{mnk}(x,\xi,\omega'_{mnk})}{\ell_{mk}(\xi)\ell_{nk}(x)[\beta_{mk}(\xi)+\beta_{nk}(x)]} \\ &\times \exp\left\{i\omega'_{mnk}[\tau_{nk}(x)-\tau_{mk}(\xi)]\right\}\; \exp\left\{i\omega''_{mnk}t\right\} dx d\xi \end{aligned} \tag{15}$$

where

$$\omega'_{mnk} \;=\; \omega\, \frac{2}{\beta_{mk}(\xi)+\beta_{nk}(x)} \;\approx\; \omega\left[1+\frac{1}{2}\left(\frac{V_m}{a}\cos\theta_{mk}(\xi) + \frac{V_n}{a}\cos\theta_{nk}(x)\right)\right] \tag{16}$$

is the Doppler-shifted frequency and

$$\omega''_{mnk} \;=\; \omega'_{mnk}[\beta_{mk}(\xi) - \beta_{nk}(x)] \;\approx\; \omega\left[\frac{V_n}{a}\cos\theta_{nk}(x) - \frac{V_m}{a}\cos\theta_{mk}(\xi)\right] \tag{17}$$

is a frequency of oscillation due to the non-stationarity of the sensor correlation. Equations 16 and 17 relate to the second and third sources of non-stationarity, respectively, discussed in Section II.A.

In attempting to connect the source cross-spectral density $Q_{mnk}(x, \xi, \omega)$ to the sensor XWVS we face two complications: the timewise oscillation of the XWVS described by the last exponential term of Eq. 15 and controlled by ω''_{mnk} of Eq. 17; and the Doppler-shifted frequency of Eq. 16. With regards to the time oscillation due to non-stationarity, considering sensor μ traveling with speed V_μ with all the other sensors being fixed, it is evident from Eq. 17 that the oscillation is suppressed when

$$V_\mu T << \frac{\lambda}{\pi\cos\theta_{\mu k}} \tag{18}$$

where λ is the acoustic wavelength. Here we see of a refined version of the non-dimensional constraint introduced in Section II.A. For polar angles significantly greater or significantly less than 90°, the block time T should be selected such that the sensor travels a distance much smaller than the acoustic wavelength to be resolved. A more quantitative version of Eq. 18 can be formulated by imposing that $|\omega''_{mnk}T/2| < \pi/6$, resulting in

$$V_\mu T \;\leq\; \frac{\lambda}{6\cos\theta_{\mu k}} \tag{19}$$

The constraint on the travel length of the sensor poses a challenge at high frequency where λ is small. At a reasonable sampling rate, the resulting block time may contain too few samples to accurately compute the the auto- or cross-spectral density. Further, if the block time is selected based on the highest frequency to be resolved, it would unnecessarily compromise the results at lower frequencies where longer block times are acceptable. This motivates the consideration of frequency-dependent windowing of the signal within a block, with the block length set to meet the approximations of Eq. 6, a condition that is much less stringent than that of Eq. 19.

Frequency-dependent windowing, or time localization, is applied to the scanning sensors only. It entails multiplication of the signal within each block by a window $g(t, \omega)$ that satisfies the energy preservation

$$\int_{-T/2}^{T/2} |g(t,\omega)|^2 dt \;=\; T \tag{20}$$

Here we select a Gaussian window of the form

$$g(t,\omega) \;=\; A(\omega)\exp\left\{-\left[\frac{t}{\delta(\omega)}\right]^2\right\} \tag{21}$$

where $\delta(\omega)$ is a time scale that declines with frequency. Applying the condition of Eq. 20,

$$A(\omega) = \left(\frac{2}{\pi}\right)^{1/4} \sqrt{\frac{T}{\delta(\omega)} \frac{1}{\operatorname{erf}\left(\frac{T}{\sqrt{2}\,\delta(\omega)}\right)}} \tag{22}$$

Figure 3 illustrates the concept of frequency-dependent windowing of the signal. In this study the time scale was chosen as $\delta \sim 1/\omega$. Although the windowing performed here bears some similarity to the S-transform and its variants [20, 21], the signal processing is quite different from those works as the focus here is on spectral estimation rather than the transform itself. The windowing of the signal was performed simultaneously with the computation of the auto- and cross-spectral densities, exploiting the further segmentation of the signal (within each block) for power spectral estimation. The detailed procedure is presented in Appendix A.

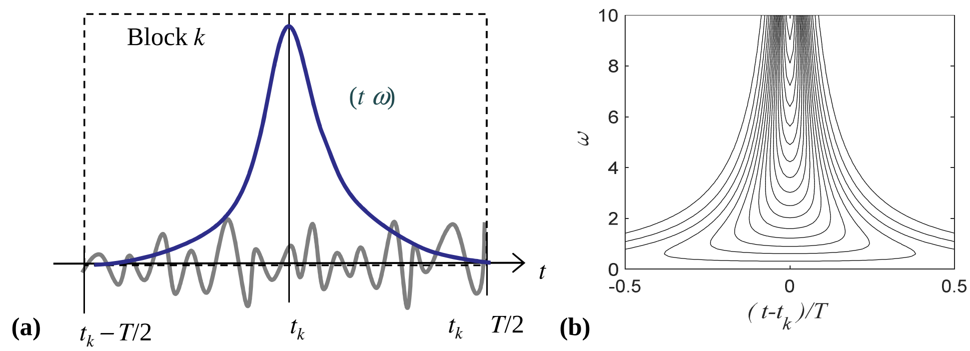

Fig. 3 Illustration of frequency-dependent windowing of the signal within a given block. (a) The window at fixed frequency; (b) representative contour map of the Gaussian window of Eqs. 21 and 22, with contour levels increasing uniformly inward.

With regards to the Doppler-shifted frequency of Eq. 16, for sufficiently slow scan Mach number it is close enough to ω to set $Q_{mnk}(x,\xi,\omega'_{mnk}) = Q_{mnk}(x,\xi,\omega)$ with very small error. On the other hand, the difference between ω'_{mnk} and ω can be significant enough at high frequency to introduce non-negligible phase changes in the second exponential term of Eq. 15. Therefore, it is prudent to leave that term as it is. Finally, since $|\alpha_{mk}| << 1$ the approximation $\beta_{mk} + \beta_{nk} = 2$ in the denominator of Eq. 15 can be made with little loss in accuracy.

Having addressed the contributions of non-stationarity, Eq. 15 is approximated as

$$G_{mnk}(\omega) = \int_{\mathcal{L}} \int_{\mathcal{L}} \frac{Q_{mnk}(x,\xi,\omega)}{\ell_{mk}(\xi)\ell_{nk}(x)} \exp\left\{i\omega'_{mnk}[\tau_{nk}(x) - \tau_{mk}(\xi)]\right\}\, dx d\xi \tag{23}$$

It is further assumed that $G_{mnk}(\omega)$ can be accurately estimated from the usual procedure

$$G_{mnk}(\omega) = \overline{P_{mk}(\omega) P^*_{nk}(\omega)}$$

where $P_{mk}(\omega)$ is the Fourier transform of $p_{mk}(t)$ and $\overline{(\,)}$ indicates the averaging of PP^*, including the Gaussian windowing of the scanning-microphone signals, over a number of segments. The time localization entails a frequency-dependent size of the Fast Fourier Transform (FFT) used in the power spectral estimation, as explained in Appendix A. This is accomplished by computing the cross-spectral densities for a number of FFT sizes, then assembling the results into a composite noise source map.

G. Model for the Coherence of the Acoustic Field

Further evaluation of Eq. 23 requires a model for the cross-spectral density of the source $Q_{mnk}(x,\xi,\omega)$. We follow the development in Ref. [14] and set

$$Q_{mnk}(x,\xi,\omega) \;=\; \psi(x,\omega)\,\Theta_{mnk}(x,\xi,\omega)\,\delta(x-\xi) \tag{24}$$

thus modeling the source as spatially incoherent (a line of uncorrelated point sources). $\Theta_{mnk}(x,\xi,\omega)$ is a directivity matrix, which can be conveniently set to

$$\Theta_{mnk}(x,\xi,\omega) \;=\; \sqrt{G_{mmk}(\omega)G_{nnk}(\omega)}\;\ell_{mk}(\xi)\ell_{nk}(x) \tag{25}$$

In this step, the directivity of the acoustic emission is accounted for through knowledge of the autospectra G_{mmk} and G_{nnk}. On defining the complex coherence of the acoustic field as

$$\gamma_{mnk}(\omega) \;\equiv\; \frac{G_{mnk}(\omega)}{\sqrt{G_{mmk}(\omega)G_{nnk}(\omega)}} \tag{26}$$

insertion of the above source model (Eqs. 24 and 25) into Eq. 23 yields

$$\gamma_{mnk}(\omega) = \int_{\mathcal{L}} \psi(x,\omega)\exp\left\{i\omega'_{mnk}[\tau_{nk}(x)-\tau_{mk}(x)]\right\}dx \tag{27}$$

For the analysis that follows, we introduce the array *response matrix*

$$Z_{mnk}(x_0,\omega) \;=\; \exp\left\{\,i\omega'_{mnk}[\tau_{nk}(x_0)-\tau_{mk}(x_0)]\,\right\} \tag{28}$$

It describes the modeled coherence of the acoustic field for a point source at $x = x_0$, that is, $\psi(x) = \delta(x-x_0)$. Equation 27 then takes the form

$$\gamma_{mnk}(\omega) = \int_{\mathcal{L}} Z_{mnk}(x,\omega)\,\psi(x,\omega)dx \tag{29}$$

where $\psi(x,\omega)$ is the *coherence-based* noise source distribution. Equation 29 represents a model for the coherence of the acoustic field and constitutes the basis for the solutions that will follow. The diagonal terms of satisfy

$$\int_{\mathcal{L}} \psi(x,\omega)dx \;=\; 1 \tag{30}$$

This is an important property of the coherence-based noise source that should be kept in mind when examining its spatial distribution. It will also prove essential in the development of a Bayesian-based inversion method.

Once the coherence-based noise source distribution is known, the *spectrum-based* source distribution for a particular sensor polar angle θ_{mk} is calculated from

$$\Psi(x,\omega,\theta_{mk}) \;=\; \psi(x,\omega)\,\Theta_{mmk}(x,x,\omega) \;=\; \psi(x,\omega)\,G_{mmk}(\omega)\,\ell^2_{mk}(x) \tag{31}$$

It is evident from Eqs. 28 and 30 that axial integration of $\Psi(x,\omega,\theta_{mk})/\ell_{mk}(x)^2$ gives the auto-spectrum $G_{mmk}(\omega)$:

$$\int_{\mathcal{L}} \frac{1}{\ell_{mk}(x)^2}\Psi(x,\omega,\theta_{mk})dx \;=\; G_{mmk}(\omega)\int_{\mathcal{L}} \psi(x,\omega)dx \;=\; G_{mmk}(\omega) \tag{32}$$

This provides a self-consistent formulation for a directional noise source [14].

III. Inversion Methods

Inversion of the integral of Eq. 29 requires first a careful accounting of the distinct values of the microphone correlations over all the blocks. Then, two inversion approaches are considered: conjugate gradient minimization and Bayesian-based estimation.

A. Assembly of Blocks

We seek the number of independent elements of the coherence matrices represented by the left-hand side of Eq. 29. For M sensors, each coherence matrix has $(M^2 - M)/2$ distinct off-diagonal elements and one distinct diagonal element (all the diagonal elements equal 1). The off-diagonal elements contain real and imaginary parts, rendering the total number of independent elements equal to $M^2 - M + 1$. Supposing that M_f sensors are fixed and M_s sensors are scanning, the total number of independent elements can be expressed as

$$J_1 \;=\; (M_f + M_s)^2 - (M_f + M_s) + 1 \;=\; M_f^2 - M_f + 1 \;+\; M_s(M_s + 2M_f - 1)$$

When segmenting the signal into blocks, the above equation gives the total number of independent elements for a given block. The first three terms on the right hand side represent the contributions of the fixed sensors; these will be the same for all the blocks. The remaining terms represent the independent elements associated with the scanning sensors at the center time of a given block. Figure 4 illustrates this concept with $M_f = 4$ and $M_s = 2$.

As we proceed from block to block, the part of the matrix contributed by the fixed sensors remains unchanged. Only the elements arising from the moving sensors change, illustrated by the colored regions in Fig. 4. For a total of K blocks, the total number of independent elements therefore is

$$J \;=\; M_f^2 - M_f + 1 \;+\; K M_s (M_s + 2M_f - 1) \tag{33}$$

Equation 29 is now written in terms of those independent elements:

$$\gamma_j(\omega) = \int_{\mathcal{L}} \psi(x,\omega) Z_j(x,\omega)\, dx \;\;, \quad j = 1, \ldots, J \tag{34}$$

On dividing the source axis into N_x uniform increments dx, at given frequency Eq. 34 is discretized by setting

$$\psi(x,\omega) \to \;\psi_i$$

$$Z_j(x,\omega)dx \to \;Z_{ji}$$

resulting in

$$\gamma_j = \sum_{i=1}^{N_x} \psi_i Z_{ji} \;, \;\; j = 1, \ldots, J \tag{35}$$

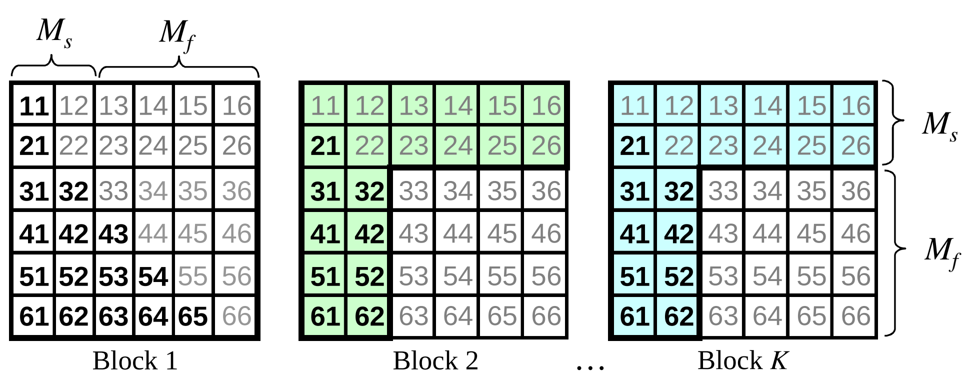

Fig. 4 Illustration of the independent elements (bold) of the coherence matrices arising from $M_f = 4$ fixed sensors and $M_s = 2$ scanning sensors. Colored areas indicate the elements that vary from one block to the next. Off-diagonal elements comprise real and imaginary components. Diagonal elements are all equal to 1.

B. Conjugate Gradient Minimization

In Eq. 34 (or its discrete version, Eq. 35), the left- and right-hand sizes represent the actual (measured) and modeled coherence fields, respectively. In the conjugate gradient approach, we seek the source distribution $\psi(x,\omega)$ that minimizes, in a least squares sense, the difference between the actual and modeled coherence fields. Given that negative sources are not physical, a non-negative constraint [15] is added by expressing the sources as

$$\psi_i \;=\; b_i^2$$

We then construct the cost function

$$F(b_i) \;=\; \frac{1}{J}\sum_{j=1}^{J}\left|\gamma_j - \sum_{i=1}^{N_x} b_i^2 Z_{ji}\right|^2 \tag{36}$$

where J is given by Eq. 33. The minimization was done iteratively using the restarted conjugate gradient method of Shanno and Phua [22]. The error was quantified in terms of the L_2 norm of the difference between the measured and modeled coherence fields, and was near 0.1.

Given that imaging of the sources of interest requires N_x on the order of 200-500, the conjugate gradient method is computationally expensive as it entails calculation of the gradient in N_x directions and for a number of function calls, for each frequency. Typically 70 function calls were required to achieve convergence. The method is practically feasible when examining a moderate number of frequencies (i.e., narrow frequency range or coarse resolution of the frequency vector), but requires very long run times when processing the entire range of a high-definition spectrum.

C. Bayesian Estimation

Bayesian estimation approaches have found wide application in the acoustic inversion problem. Originally developed for astronomical image restoration, the Richardson-Lucy algorithm [23, 24] is a Bayesian-based iterative method that had been applied to the deconvolution of noise source maps obtained by beamforming [14, 25]. Recent works have proposed Bayesian formulations for minimizing the cost functional based on its maximum a posteriori estimation [26–28]. Here we apply a simple Bayesian estimation method directly to the the integral for the modeled coherence field, Eq. 34. Detailed background is provided in Appendix B.

Considering a convolution integral of the type

$$\phi(\xi) \;=\; \int \psi(x)P(\xi,x)dx$$

Bayesian estimation seeks inversion by treating the variables involved (after appropriate scaling, where necessary) as probability density functions (pdfs): conditional pdf for $P(\xi,x)$ and total pdfs for $\phi(x)$ and $\psi(x)$. In traditional beamforming, $P(\xi,x)$ is the point spread function. The integral of Eq. 34 seems like an unlikely candidate for this approach. However, through some simple manipulations, it will be shown that it can indeed be treated by the Bayesian estimation. First, the index $j = 1, \ldots, J$ can be thought of as a discrete representation of a continuous virtual coordinate ξ. The mapping between ξ and j is arbitrary as the ordering of j does not affect the evaluation of of Eq. 34. Then, at fixed frequency, Eq. 34 takes the form

$$\gamma(\xi) = \int_{\mathcal{L}} \psi(x) Z(\xi, x)\, dx \tag{37}$$

A further difficulty arises from the fact that pdfs are supposed to be non-negative, however both γ and Z range between -1 and 1. This is easily overcome by adding Eq. 30 to Eq. 37, yielding

$$1 + \gamma(\xi) = \int_{\mathcal{L}} \psi(x)[1 + Z(\xi, x)]\, dx \tag{38}$$

We note that $1 + \gamma$ and $1 + Z$ are both non-negative, so the above integral now becomes a candidate for the Bayesian estimation approach. Its discrete version is

$$1 + \gamma_j = \sum_{i=1}^{N_x} \psi_i (1 + Z_{ji}) \tag{39}$$

Using the relations presented in Appendix B, Eq. 39 is inverted through the iterative scheme

$$\psi_i^{(l+1)} = \frac{\psi_i^{(l)}}{\sum_{j=1}^{J}(1 + Z_{ji})} \sum_{j=1}^{J} \frac{(1 + \gamma_j)(1 + Z_{ji})}{\sum_{i=1}^{N_x} \psi_i^{(l)} (1 + Z_{ji})} \tag{40}$$

where l denotes the iteration step. Typically 2000 iterations were required to achieve convergence to an error (L_2 norm of the difference between the measured and modeled coherence fields) of around 0.1. The Bayesian estimation gave results very similar to those calculated by the conjugate gradient minimization, and was at least an order of magnitude faster. Thus, most of the results presented in this paper are based on the Bayesian estimation.

IV. Experimental Setup

A. Phased Microphone Array

Noise measurements were conducted in the UCI aeroacoustic facility depicted in Fig. 5. A microphone phased array consists of up to twenty-four 1/8 in. condenser microphones (Brüel & Kjaer, Model 4138) with frequency response up to 120 kHz. The microphones are connected, in groups of four, to six conditioning amplifiers (Brüel & Kjaer, Model 2690-A-0S4). The outputs of the amplifiers are sampled simultaneously, at 250 kHz per channel, by three 8-channel multi-function data acquisition boards (National Instruments PCI-6143) installed in a Dell Precision T7400 computer with a Xeon quad-core processor. National Instruments LabVIEW software is used to acquire the signals.

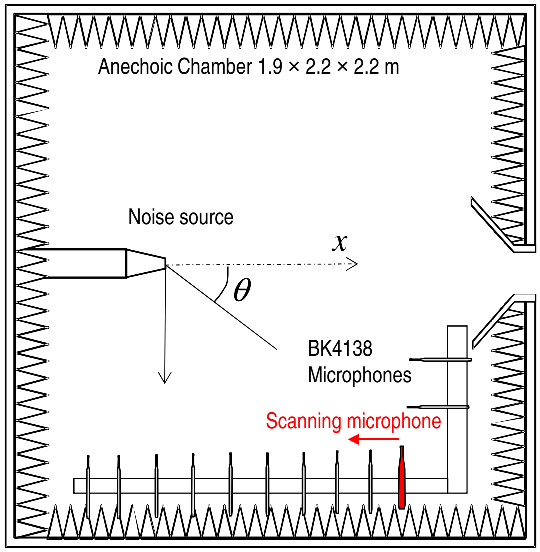

Fig. 5 Anechoic chamber. Scanning microphone is indicated in red.

The temperature and humidity inside the anechoic chamber are recorded to enable computation of atmospheric absorption and the exact speed of sound. The microphone signals are conditioned with a high-pass filter set at 300 Hz. Narrowband sound pressure level (SPL) spectra are typically computed using a 2048-point Fast Fourier Transform, yielding a frequency resolution of 122 Hz. The spectra are corrected for microphone actuator response, microphone free field response and atmospheric absorption, thus resulting in lossless spectra.

In the present study, a total of 13 microphones were used, covering a polar sector from $\theta = 42°$ to $\theta = 73°$. One continuous-scan microphone was mounted on a linear traverse consisting of a belt drive (Igus ZLW-0630) powered by a servo motor (ClearPath-MCPV). The design of the traverse system is depicted in Fig. 6. The path of the traverse was parallel to the line of the twelve fixed microphones that were mounted on the horizontal arm of the array holder depicted in Fig. 6. The scanning and fixed microphones had offset distances of 6 mm, as illustrated in Fig. 7.

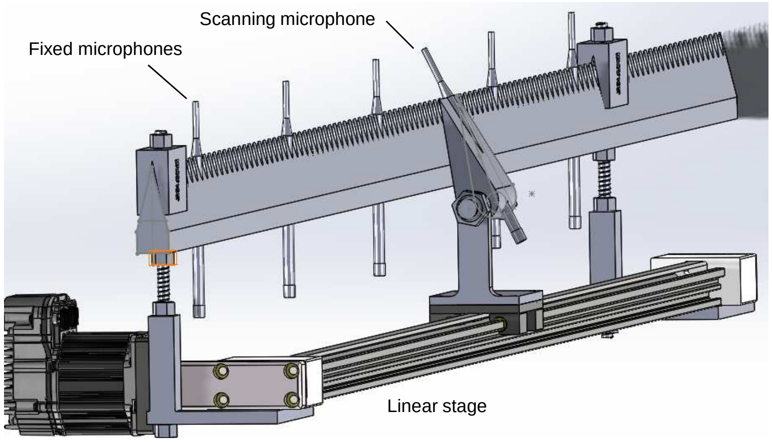

Fig. 6 Design of linear traverse system.

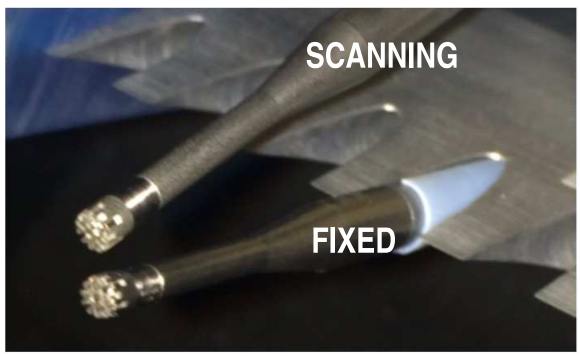

Fig. 7 Fixed and scanning microphones at their closest spacing of 6 mm, measured from the cartridge centers.

The servo motor was programmed to rotate at fixed RPM, moving the linear stage at constant speed towards the source, with a stroke length of 580 mm and speed of 69.3 mm/s. The Mach number of the scanning microphone was 0.00020. A total of 2100000 data points (8.4 s) were acquired for each microphone data record. Through synchronization of the microphone signal acquisition with the triggering of the servo motor, the position of the moving microphone was known to within approximately one millimeter.

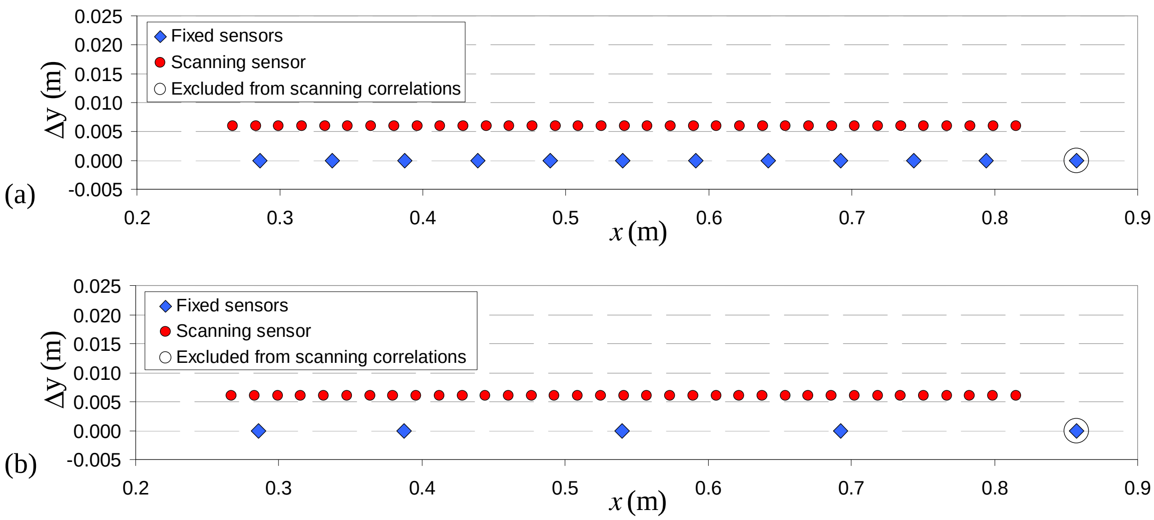

Fig. 8 Array configurations: (a) full; (b) partial. Scanning sensor is shown at the block center times t_k. Circled sensor was excluded from the scanning correlations to maintain equal sensor count.

Figure 8 presents the geometric deployments of the fixed and scanning microphones for two array configurations, full and partial. The transverse coordinate is referenced to the line of the fixed sensors. For both configurations, when conducting the scanning correlations, the signals were divided into 35 blocks with 50% overlap. Each block contained 122880 samples, corresponding to a duration of 0.49 s and sensor travel of 34.1 mm. The selected block duration provided sufficient points for the accurate estimation of spectra and satisfied the criteria of the last two lines of Eq. 6: the source-to-observer distance varied by no more than 1%, and the polar angle varied by no more than 2°. It was verified that this variation of polar angle produced negligible change in the variance of the acoustic field for the sources studied here. For the scanning correlations, the downstream-most microphone was excluded to maintain the same sensor count when comparing results of scanning and fixed configurations. The full configuration utilized all 13 of the available microphones (with the aforementioned exclusion): 11 fixed plus one scanning (F11S01) or 12 fixed (F12). The partial configuration involved only six microphones to demonstrate the benefits of scanning in a sparse array: four fixed plus one scanning (F04S01) or five fixed (F05). When only fixed microphones were used, the processing encompassed the entire experimental duration of 8.4 s in a single block.

Noise source maps for configurations that included the scanning microphone were constructed by combining spectral results at FFT sizes of 2048, 1024, 512, and 256, as described in Appendix A. A frequency-dependent Gaussian window with c_λ=0.2 (Eq. A3) was used. Noise source maps that involved only fixed microphones were constructed using an FFT size of 2048, and no windowing was applied.

B. Flow Visualization

Spark schlieren photography was applied to the jet flow described below. The schlieren system employed a 20-nanosecond spark gap as a light source (Xenon, Model N787B); lenses with 150-mm diameter and 1-m focal length for collimating the light beam; and a charged coupled device (CCD) camera for acquiring the images (Sony, DSCF717). A knife edge normal to the jet axis was used to cut off the light rays. The spatial resolution of the images is 2560 × 1920 pixels.

C. Noise Sources

The study examined two types of noise sources: an impinging-jets rig and an overexpanded supersonic jet. The impinging-jets rig has a design similar to that used by Gerhold *et al.* [29] and uses the collision of four jets, issuing from tubing with 2.4-mm internal diameter, to create an approximation to a point source. Figure 9 depicts the setup. The impinging jets were supplied by air at a supply pressure of 205 kPa.

The supersonic jet was supplied by a convergent-divergent nozzle, designed by the method of characteristics for Mach 1.50 exit flow. The nozzle exit diameter is D = 14.0 mm. The nozzle was supplied by air at a total pressure of 308 kPa, resulting in an over-expanded condition with fully-expanded Mach number of 1.38 and fully-expanded velocity U = 403 m/s. At this condition, the jet emits strong broadband shock noise and screech, in addition to turbulent mixing noise. To accentuate the feedback loop that sustains screech, an annular flat plate of 30-mm diameter was attached to the nozzle exit [30]. Figure 10 plots the radial coordinates of the nozzle and plate, and includes a photograph of the nozzle exit. Although a detailed analysis of shock-associated noise was outside the purview of this study, this jet was selected because it contains random (broadband) and deterministic (tonal) sources, and is thus an interesting source field on which to test the imaging techniques. A spark schlieren image of the jet is shown in Fig. 11. The shock cell structure is evident in the first few jet diameters. The initial shock-cell spacing (first two interactions of the shocks with the shear layer) is ~ 22 mm (0.9D).

For both sources, support structures in the vicinity of the source origin were covered with anechoic foam to minimize reflections.

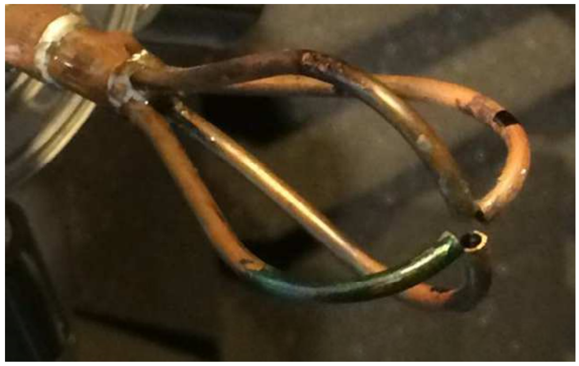

Fig. 9 Impinging jets source.

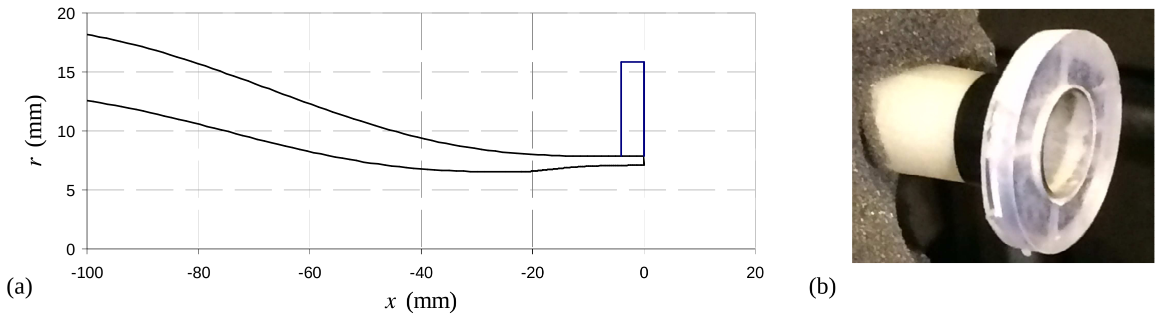

Fig. 10 Convergent-divergent nozzle with annular end plate for generation of screeching overexpanded jet: (a) radial coordinates; (b) photograph of exit.

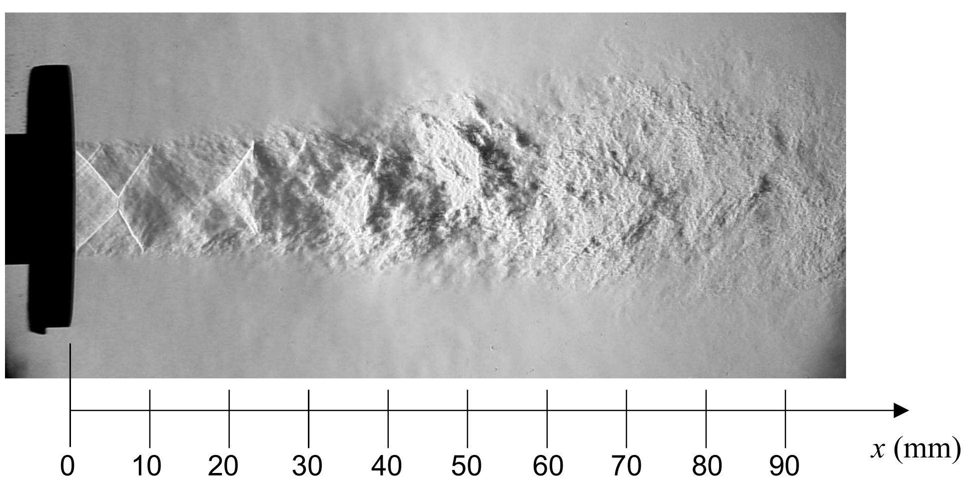

Fig. 11 Spark schlieren image of the overexpanded jet.

V. Results

Acoustic results will be presented for the two sources described above. The results encompass sound pressure level spectra and noise source maps using the direct spectral estimation methods described in Section II and Appendix A. In addition, results from “conventional" beamforming using the delay-and-sum method, as implemented in Ref. Papamoschou [14], will be included.

A. Impinging Jets

Figure 12 plots SPL spectra for the impinging-jets source, measured with the fixed microphones, at various polar angles θ. The spectra are broadband and peak at a frequency near 40 kHz. The emission is moderately directive, the spectral peak increasing by $\sim$ 3 dB from $\theta = 47.8°$ to $\theta = 72.7°$. Figure 13 compares three coherence-based noise source maps for the full array configuration of Fig. 8(a): delay-and-sum, using the fixed sensors only (F12); Bayesian estimation using the fixed sensors only (F12); and Bayesian estimation using the fixed and scanning sensors (F11S01). The delay-and-sum map shows strong sidelobes and a blurred map. The Bayesian estimation with F12 results in a sharp map with suppressed, but still visible, sidelobes. Bayesian estimation with F11S01 results in a map that has similar spatial resolution as with F12 and is practically devoid of sidelobes. Note that the source levels for delay-and-sum are much lower than those associated with Bayesian method. This is the result of the conservation principle of Eq. 30, and the fact that the delay-and-sum map is spread out because of blurring and side lobes.

To provide more detail on the performance of the imaging methods, Fig. 14 plots the distribution of ψ, normalized by its peak value, at $f = 50$ kHz for delay-and-sum, Bayesian estimation with F12, and Bayesian estimation with F11S01. The superior spatial resolution of the direct spectral estimation methods against delay-and-sum is evident. Even though the Bayesian maps with F12 and F11S01 have similar spatial resolution, the F12 maps shows a double-peak distribution that is not deemed physical. Even though the tubular support structure of the impinging-jets setup (Fig. 9) will cause some reflections, the tubes are too slender for these reflections to cause a peak of comparable amplitude as the source itself. Further, the secondary apparent source, with the lower peak, is located away from the tubes, making it even more improbable it was caused by reflections. The F11S01 map shows a single peak and is thus considered to have higher fidelity. The slight negative offset ($\sim$ 7 mm) of the peak from its expected location at $x = 0$ m is likely due to small errors in the geometric calibration of the microphone array.

The suspected unphysical result yielded by configuration F12 may relate to the spacing of the fixed sensors. Ideally, the sensor deployment would be such as to adequately sample the spatial variation of the measured coherence field, which is governed by the array response matrix of Eq. 28. This spatial pattern is complex, but it is fair to say that it has a characteristic wavelength of the same order as the acoustic wavelength λ. Sufficient spatial sampling at high frequency (short wavelenghth) would require a very dense array, which is impractical. Spatial under-sampling introduces uncertainty whose effects may be amplified when detecting a highly localized source like the impinging-jets source. It is evident from Fig. 8a that F11S01 improves spatial sampling relative to F12 by introducing closely-spaced measurement points between a given fixed microphone and the scanning microphone. This in fact is a significant benefit of the continuous-scan paradigm as implemented in our study.

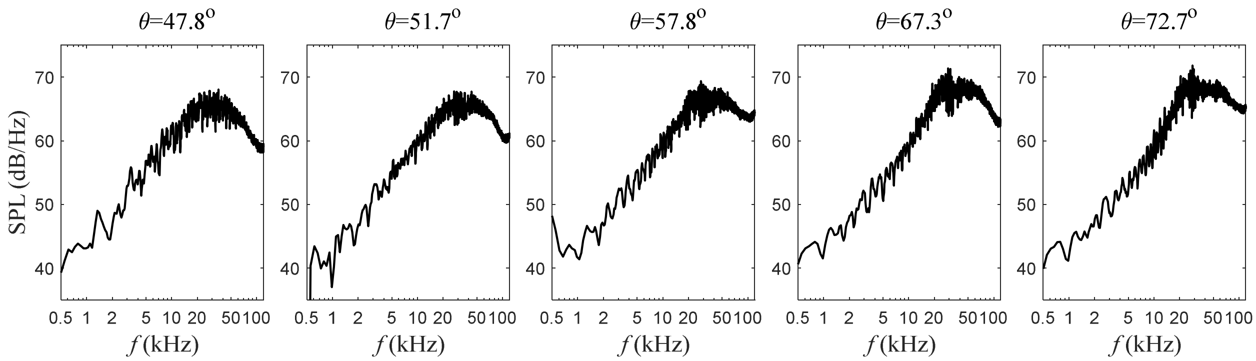

Fig. 12 SPL spectra for the impinging-jets source source at various polar angles. The spectra are referenced to a radius of 0.305 m.

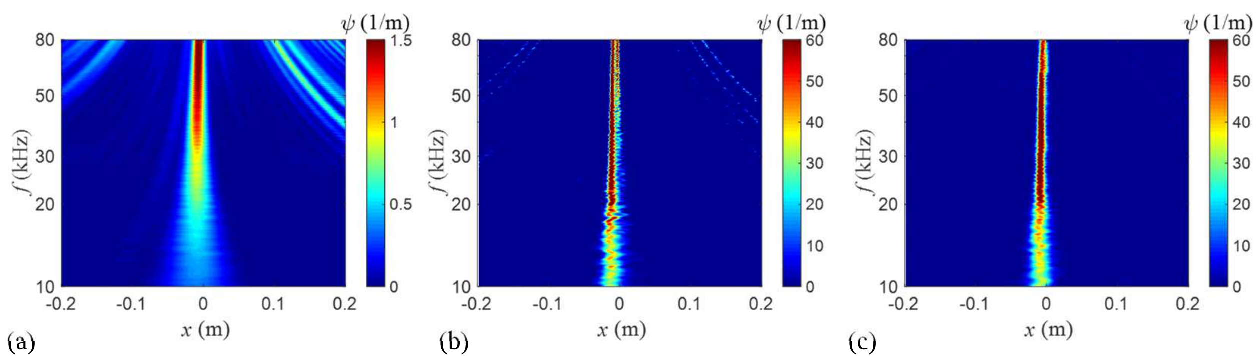

Fig. 13 Coherence-based source strength $\psi(x,\omega)$ for the impinging-jets source using the full array configuration of Fig. 8(a). (a) Delay-and-sum (F12); (b) Bayesian estimation (F12); (c) Bayesian estimation (F11S01).

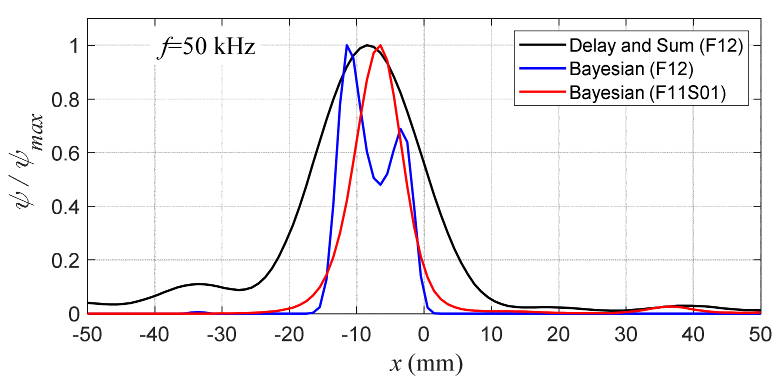

Fig. 14 Axial distributions of coherence-based source strength $\psi(x,\omega)$, normalized by peak value, for the impinging-jets source at 50 kHz.

B. Overexpanded Jet

The SPL spectra for the overexpanded jet, measured with the fixed microphones, are presented in Fig. 15. The effects of screech and broadband shock noise are evident. A screech tone near 10 kHz dominates most of surveyed polar sector, with exception of the highest angles where the second harmonic near 20 kHz overtakes. The screech Strouhal number is $Sr = fD/U = 0.35$, in line with the correlations found in Raman [30] for jets at similar fully-expanded Mach number. The spectra are highly directional, with the screech tones undergoing significant variations with polar angle.

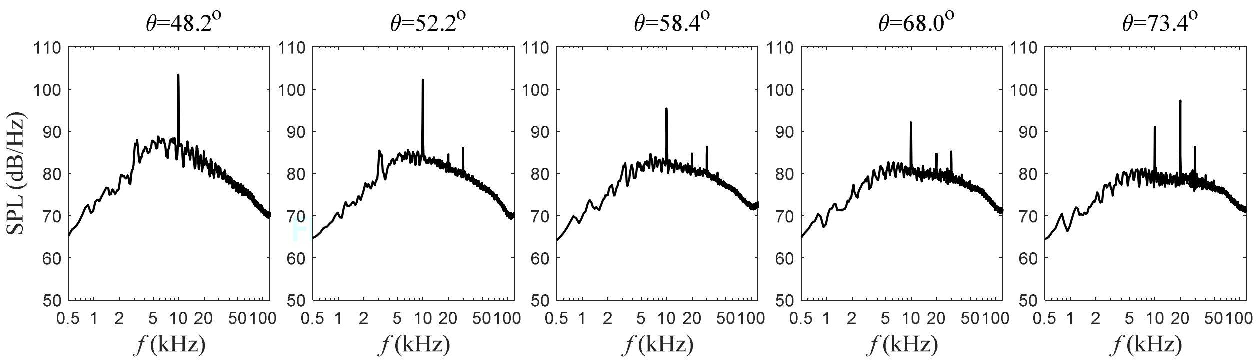

Fig. 15 SPL spectra for the overexpanded jet at various polar angles. Spectra are referenced to a radius of 0.305 m.

Figure 16 presents three coherence-based noise source maps for the full array configuration of Fig. 8(a): delay-and-sum, using the fixed sensors only (F12); Bayesian estimation using the fixed sensors only (F12); and Bayesian estimation using the fixed and scanning sensors (F11S01). Similar to the impinging-jet maps discussed above, the delay-and-sum map suffers from strong sidelobes and limited spatial resolution. The screech tones are evident, but their spatial features are smeared. Bayesian estimation with F12 improves significantly the spatial resolution and generally suppresses the sidelobes, although an appreciable sidelobe at high frequency is still noted. Bayesian estimation with F11S01 suppresses considerably all the sidelobes. The map has a little more speckle at high frequency than for F12, which could be an effect of non-stationarity that will be addressed in future studies.

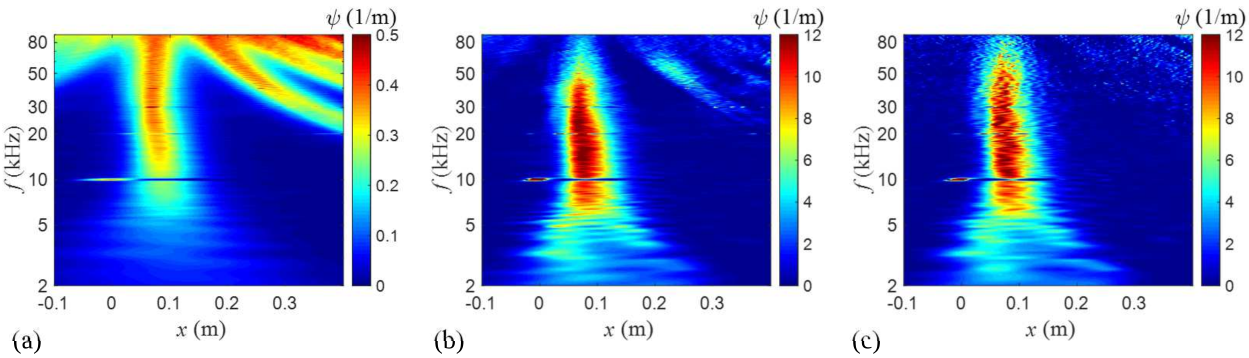

Fig. 16 Coherence-based source strength $\psi(x,\omega)$ for the overexpanded jet using the full array configuration of Fig. 8(a). (a) Delay-and-sum (F12); (b) Bayesian estimation (F12); (c) Bayesian estimation (F11S01).

It is instructive to examine the source distributions of Fig. 16 near the screech tone of 10 kHz. This is done in Fig. 17. The delay-and-sum method provides poor spatial definition of the source. The Bayesian estimation applied to F12 shows clearly a spatially-periodic pattern of sources, corresponding to the screech generation and the reflection from the plate. These features become sharper and better defined when the Bayesian estimation is applied to F11S01. The suppression of broadband level of the coherence-based noise source at the screech tone, evident in Fig. 17, is a consequence of the constraint of Eq. 30. That is, the occurrence of sharp peaks must be accompanied by suppression of broadband levels so that the integral of Eq. 30 is preserved. The spectrum-based noise source distributions, to be presented in Figs. 20-21, preserve the broadband levels.

Figures 18 and 19 present results analogous to those of Figs. 15 and 16, respectively, for the sparse array of Fig. 8(b). Here the delay-and-sum result is dominated by sidelobes and provides little useful information, while the Bayesian estimation with fixed sensors (F05) results in a scattered map with strong sidelobes. The maps near the screech tone suffer from strong ghost images. However, when the Bayesian estimation is applied to F04S01, a map with similar quality to that of the full array F11S01 emerges. This underscores the ability of the continuous scan method, coupled with the methodology developed here, to provide high resolution maps with low sensor count. Specifically, we have demonstrated noise source maps of similar quality and resolution using less than half the number of sensors (5) compared with the baseline experiment (12).

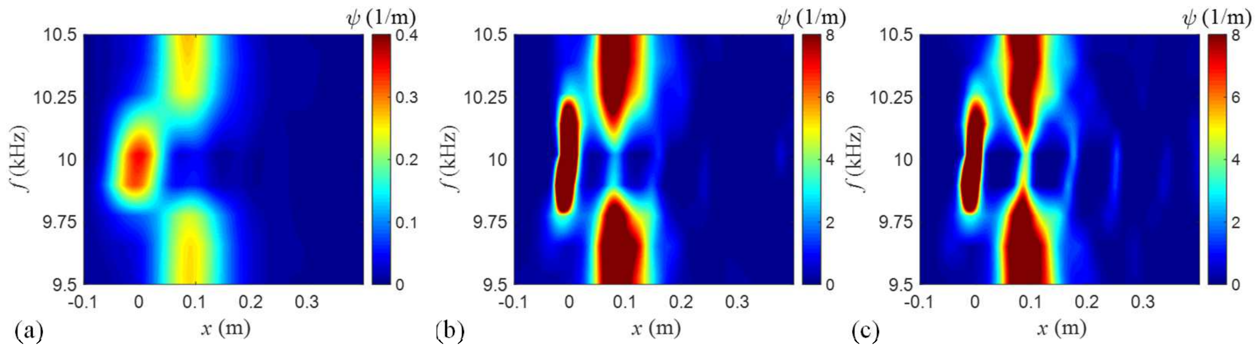

Fig. 17 Detail of coherence-based source strength $\psi(x, \omega)$ for the impinging-jets source using the full array configuration of Fig. 8(a). (a) Delay-and-sum (F12); (b) Bayesian estimation (F12); (c) Bayesian estimation (F11S01).

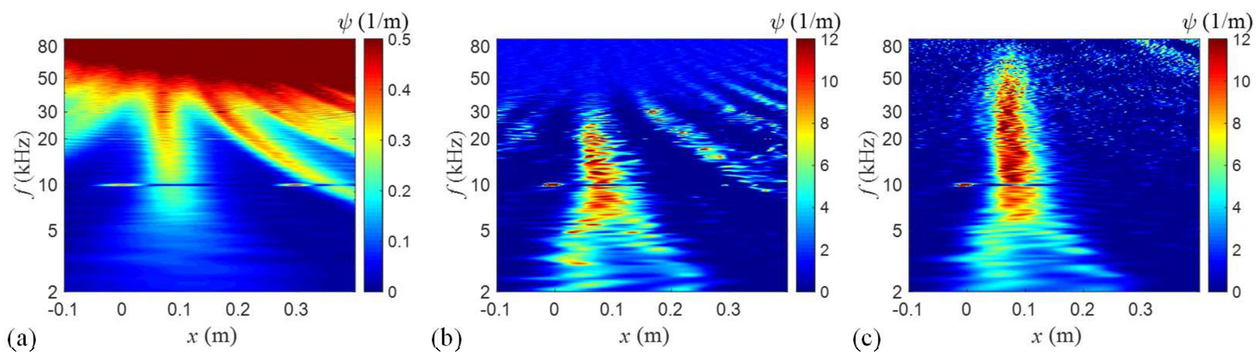

Fig. 18 Coherence-based source strength $\psi(x, \omega)$ for the overexpanded jet using the partial array configuration of Fig. 8(b). (a) Delay-and-sum (F05); (b) Bayesian estimation (F05); (c) Bayesian estimation (F04S01).

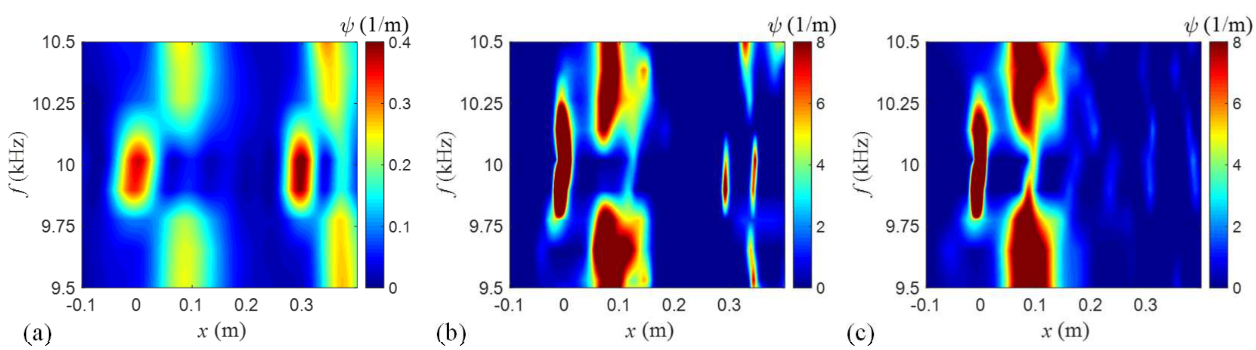

Fig. 19 Detail of coherence-based source strength $\psi(x, \omega)$ for the overexpanded jet using the partial array configuration of Fig. 8(b). (a) Delay-and-sum (F05); (b) Bayesian estimation (F05); (c) Bayesian estimation (F04S01).

Returning to the full scanning configuration F11S01, Figure 20 plots the spectrum-based noise source, obtained from Eq. 31, at microphone polar angle $\theta = 52°$. The noise source maps, now in decibels, depict clearly the periodic succession of sources associated with the screech generation in the jet. Lastly, Fig. 21 compares the Bayesian-estimation results with those obtained from the conjugate-gradient minimizer. It is seen that the two techniques produce very similar maps, with the Bayesian estimation giving slightly sharper images of the source field.

Concerning the connection of the aforementioned results (particularly Figs. 20 and 21) to the screech problem, the most prominent noise source is at $x/D = 0$ where the reflector plate is located. The first downstream peak is at $x/D \approx 6$ (approximately six shock cells donwtream of the nozzle exit), which is in line with the general expectation of the source location for the screech tone for a jet at this Mach number [31, 32]. The first peak coincides with the location of broadband noise. It is followed by a second peak at $x/D \approx 12$ that is about 6 dB weaker. Although the significance of the second peak is not presently clear, it is noteworthy that a similar pattern has been observed in the beamforming maps of an underexpanded jet by Dougherty and Podboy [33]. In the images of Figs. 19 and 20, one can identify third and fourth peaks at much diminished amplitudes. Their intensities are at least 6 dB below that of the first peak, so it is not clear if they represent real sources or ghost images.

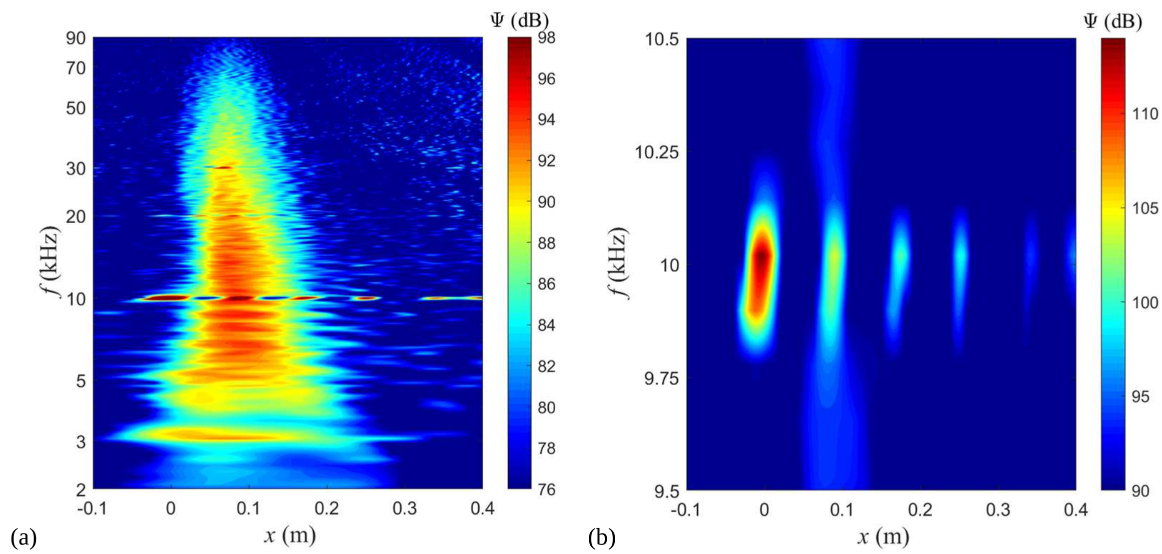

Fig. 20 Spectrum-based source strength $\Psi(x,\omega)$ for the overexpanded jet using the F11S01 array configuration and computed using Bayesian estimation. Microphone angle $\theta = 52°$. (a) Complete map; (b) detail near the screech tone at 10 kHz.

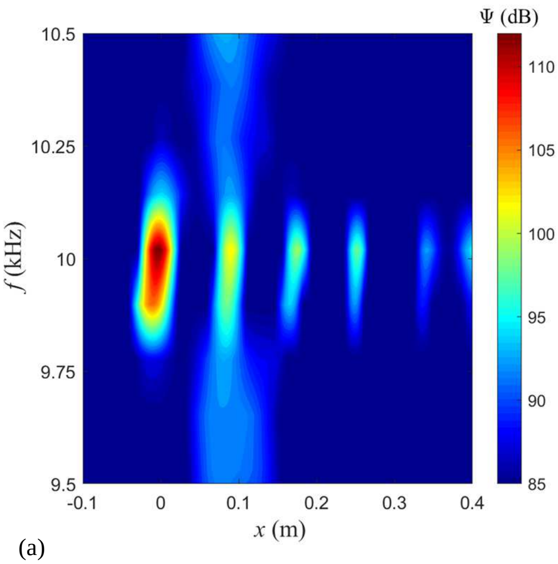

Fig. 21 Spectrum-based source strength $\Psi(x, \omega)$ for the overexpanded jet using the F11S01 array configuration, showing detail near 10 kHz. Microphone angle $\theta = 63°$. (a) Bayesian estimation; (b) conjugate gradient minimization.

The full-frequency maps shown in Figs. 16(b), 16(c), 18(c), and 20(a) indicate that the peak noise source location in the jet flow is centered around $x/D = 6$ and is fairly invariant with frequency. This suggests that the acoustic emission is dominated by shock-associated noise that emanates from specific shock cells, in contrast with turbulent mixing noise whose peak location moves toward the nozzle exit with increasing frequency (see, for example, Ref. [14]). Similar trends have been observed in phased-array acoustic imaging of a Mach 1.35 underexpended jet [28].

VI. Concluding Remarks

A methodology was presented for the direct estimation of the spatio-spectral distribution of an acoustic source from microphone measurements that comprise fixed and continuously scanning sensors. Application of the Wigner-Ville spectrum allows the quantification of the non-stationarity introduced by the sensor motion. The most challenging aspect of the non-stationarity is the time dependence of the time separation in the source space-time correlation. Suppression of the non-stationarity in the signal processing entails division of the signals into blocks and application of a frequency-dependent window within each block. In addition, frequency variation of the size of the Fast Fourier Transform is desirable to resolve sources at high frequency.

The direct estimation approach entails the inversion of an integral that connects the source distribution to the measured coherence of the acoustic field. The segmentation of the signals into blocks requires careful assembly of the distinct elements of the sensor coherence matrix over the totality of the blocks. A Bayesian-estimation approach is developed that allows for efficient inversion of the integral and performs similarly to the much costlier conjugate gradient method. The methodology is applied to acoustic fields emitted by impinging jets approximating a point source and an overexpanded supersonic jet. The measurement setup comprised one continuously scanning microphone and a number of fixed microphones, all arranged on a linear array. Comparisons are made between array configurations with fixed microphones only and with the scanning microphone, all having the same sensor count. The noise source maps with the scanning microphone have improved spatial fidelity and suppressed sidelobes. The advantage of the continuous scan paradigm is particularly strong when sparse arrays are used. Noise source maps measured with only five sensors (four fixed and one scanning) have similar quality and resolution to maps measured with 12 sensors (11 fixed and one scanning).

In addition to the benefits of increased spatial resolution and reduction in acquisition time mentioned in the Introduction, the continuous-scan approach as implemented in this study allows correlations between closely-spaced measurements points, even in a sparse deployment of fixed sensors. This improves the spatial sampling of the acoustic field, which is deemed important for high-fidelity detection of the noise source. Potential improvements to the methodology include the determination of optimal block sizes and Gaussian filter widths, as well as variable scan speeds whereby the sensor slows down near regions of interest. While the proposed Bayesian estimation approach is computationally more efficient than the conjugate gradient method, it lacks the flexibility of the latter in including constraints that can improve the realism of the source distribution. However, regularization techniques may be implemented in the Bayesian estimation method to improve the fidelity of the result [28, 34].

The present method used a one-dimensional model for the noise source; there is already work on two-dimensional noise source imaging using rotating microphone arrays in combination with fixed reference microphones [17]. The methodology presented in this paper can be extended to two-dimensional imaging that involves fixed and scanning arrays of sensors.

Appendix A: Spectral Estimation Using Frequency-Dependent Windowing

The frequency-dependent windowing discussed in Section II.E, and illustrated in Fig. 3, does not allow a straightforward transition from time domain to frequency domain. It is not possible to window the signal in time domain and then calculate the Fourier transforms that are involved in spectral estimation. If one is interested in the Fourier transform of a single time trace multiplied by a frequency-dependent window, it can be computed via convolution of the Fourier transform of the original signal with the Fourier transform of the window [20, 35]. However, this approach becomes cumbersome and expensive when it comes to spectral estimation.

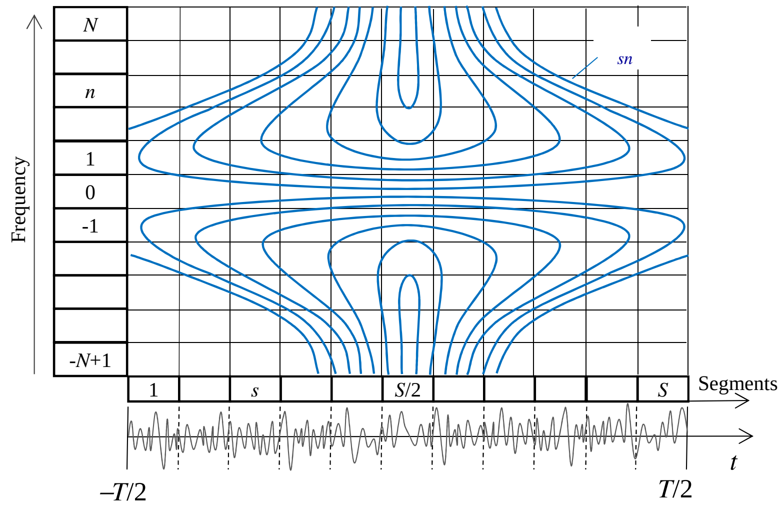

Fig. A1 Illustration of the implementation of the frequency-dependent windowing in spectral estimation of the signal in a given block.

To understand the approach employed here, it is helpful to review the basic steps involved in spectral estimation. Referring to Fig. A1, consider a time signal $p(t)$ of duration T corresponding to a given block k of the data. For convenience, set the center time of the block to $t_k = 0$. The signal is sampled at a sampling rate F_s, yielding $N_k = F_s T$ samples over the duration T. For spectral estimation, the signal is divided into S overlapping or non-overlapping segments and a Fast Fourier Transform (FFT) of size N_{FFT} is computed for each segment. The FFT algorithm imposes that the segment contain $2N_{\text{FFT}}$ samples, resulting in a segment time interval $\Delta t_{\text{seg}} = 2N_{\text{FFT}}/F_s$. Application of the FFT to segment s yields the complex-valued Fourier transform P_{sn} for $2N$ values of the frequency, where $n = -N+1, \ldots, N$ denotes the frequency index, $N = N_{\text{FFT}}/2$, and the cyclic frequency is $f_n = F_s n/(2N)$. The Nyquist frequency is $f_N = F_s/2$ and the frequency resolution is $\Delta f = F_s/N_{\text{FFT}}$.

The frequency-dependent time localization sought by the window of Eqs. 21 and 22 is accomplished by representing time in terms of the segment index s, provided there is sufficient coverage of the window width $\delta(\omega)$ by the segments. The Gaussian is centered at $s = S/2$, and the discrete representation of Eq. 21 becomes

$$g_{sn} = A_n \exp\left\{-\left(\frac{T}{\delta_n}\right)^2 \left(\frac{s}{S} - \frac{1}{2}\right)^2\right\}, \quad s = 1, \ldots, S;\; n = -N+1, \ldots, N \tag{A1}$$

where A_n is evaluated from Eq. 22. Then, the time-localized Fourier transform is

$$P_{sn}^{\text{localized}} = P_{sn}\, g_{sn}, \quad s = 1, \ldots, S;\; n = -N+1, \ldots, N \tag{A2}$$

Computation of the auto-spectral density includes the usual steps of multiplying the Fourier transform by its conjugate, then averaging over the segments while folding the negative frequencies. Cross-spectral densities are similarly evaluated.

Localization is applied only to the signals of the scanning microphones.

In selecting the parameters for the frequency-based localization, there are two considerations: minimization of the effects of non-stationarity, as expressed by Eq. 19; and sufficient coverage of $\delta(\omega)$ by the segments. The former condition can be formulated as

$$V_\mu \delta \;=\; c_\lambda\, \lambda \;=\; c_\lambda \frac{a}{|f|} \tag{A3}$$

where c_λ is the fraction of the acoustic wavelength that the sensor traverses in time δ and should be selected consistently with Eq. 19. The resulting discrete form of δ is

$$\delta_n \;=\; c_\lambda \frac{a}{V_\mu} \frac{1}{f_N} \frac{N}{\epsilon + |n|} \;\;,\;\; n = -N+1, \ldots, N \tag{A4}$$

where ϵ is a small number included to avoid singularity at zero frequency. As a fraction of the block time,

$$\frac{\delta_n}{T} \;=\; c_\lambda \frac{a}{V_\mu} \frac{1}{N_k} \frac{2N}{\epsilon + |n|} \;\;,\;\; n = -N+1, \ldots, N \tag{A5}$$

The coverage requirement is expressed as

$$\frac{\delta}{\Delta t_{\mathrm{seg}}} \;=\; c_{\mathrm{cov}} \tag{A6}$$

where c_{cov} is a number significantly greater than 1. Recalling that $\Delta t_{\mathrm{seg}} = 2N_{\mathrm{FFT}}/F_s = N_{\mathrm{FFT}}/f_N$,

$$\delta \;=\; c_{\mathrm{cov}} \frac{N_{\mathrm{FFT}}}{f_N} \tag{A7}$$

Combined with the stationarity condition of Eq. A3, this imposes a constraint on the maximum size of the FFT:

$$N_{\mathrm{FFT}} \;\leq\; \frac{c_\lambda}{c_{\mathrm{cov}}} \frac{a}{V_\mu} \frac{f_N}{|f|} \tag{A8}$$

where f is the highest frequency to be resolved. In other words, because the segment sample size equals $2N_{\mathrm{FFT}}$, the size of the FFT must be such as to ensure that the width of the Gaussian window is adequately resolved by the segment time. Therefore, the size of the FFT (an integer power of 2) must be selected in accordance with Eq. A8.

We illustrate with the conditions of the experiment described in Section IV: $f_N = 125{,}000$ Hz and $V_\mu/a = 0.00020$. It is reasonable to select $c_\lambda = 0.2$ and $c_{\mathrm{cov}} = 5$, resulting in

$$N_{\mathrm{FFT}} \;\leq\; 200 \frac{f_N}{|f|}$$

Assuming that the highest frequency of interest is $f = 90{,}000$ Hz, we must satisfy $N_{\mathrm{FFT}} \leq 278$. The closest power of two is $N_{\mathrm{FFT}} = 256$. This provides a frequency resolution $\Delta f = 976$ Hz, which may be too coarse for certain applications. A compromise is to compute the spectral densities (or noise source maps) for several N_{FFT}s, then patch the results as depicted schematically in Fig. A2.

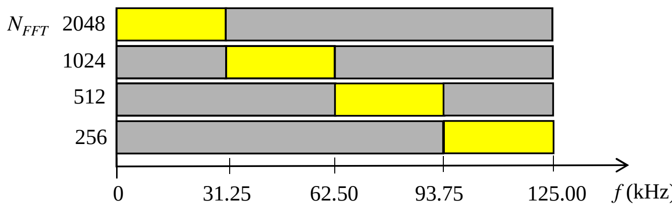

Fig. A2 Construction of composite cross-spectral density, or noise source map, by patching solutions at different N_{FFT}s. Yellow region shows selection of the frequency vector from different FFT sizes.

To appreciate the effects of frequency-based localization and FFT size, Fig. A3 presents coherence-based distributions, computed using the Bayesian estimation procedure of Section III.C, for the overexpanded jet described in Section IV.B. The microphone signals were divided into 19 non-overlapping blocks with uniform duration $T = 0.401$ s. Within each block, the scanning microphone traversed 27.7 mm, which corresponds to 7.2 wavelengths at the highest frequency of interest, 90 kHz. The effect of frequency-dependent windowing, with $c_\lambda = 0.2$, is clear when comparing Figs. A3(a) and (b). Without windowing, the noise source map loses definition at frequencies above about 28 kHz, a stark ramification of the non-stationarity discussed in Section II.E. Application of windowing extends the map definition to about 70 kHz. Reduction of the FFT size, Figs. A3(c) to (e), progressively improves the definition of the noise source map at high frequency, a result of the improved coverage of the window width discussed in connection with Eq. A6. However, resolution of fine features such as the source distribution at the screech frequency near 10 kHz degrades with decreasing FFT size. The composite map shown in Fig. A3(f) retains those fine features and allows source definition up to about 80 kHz.

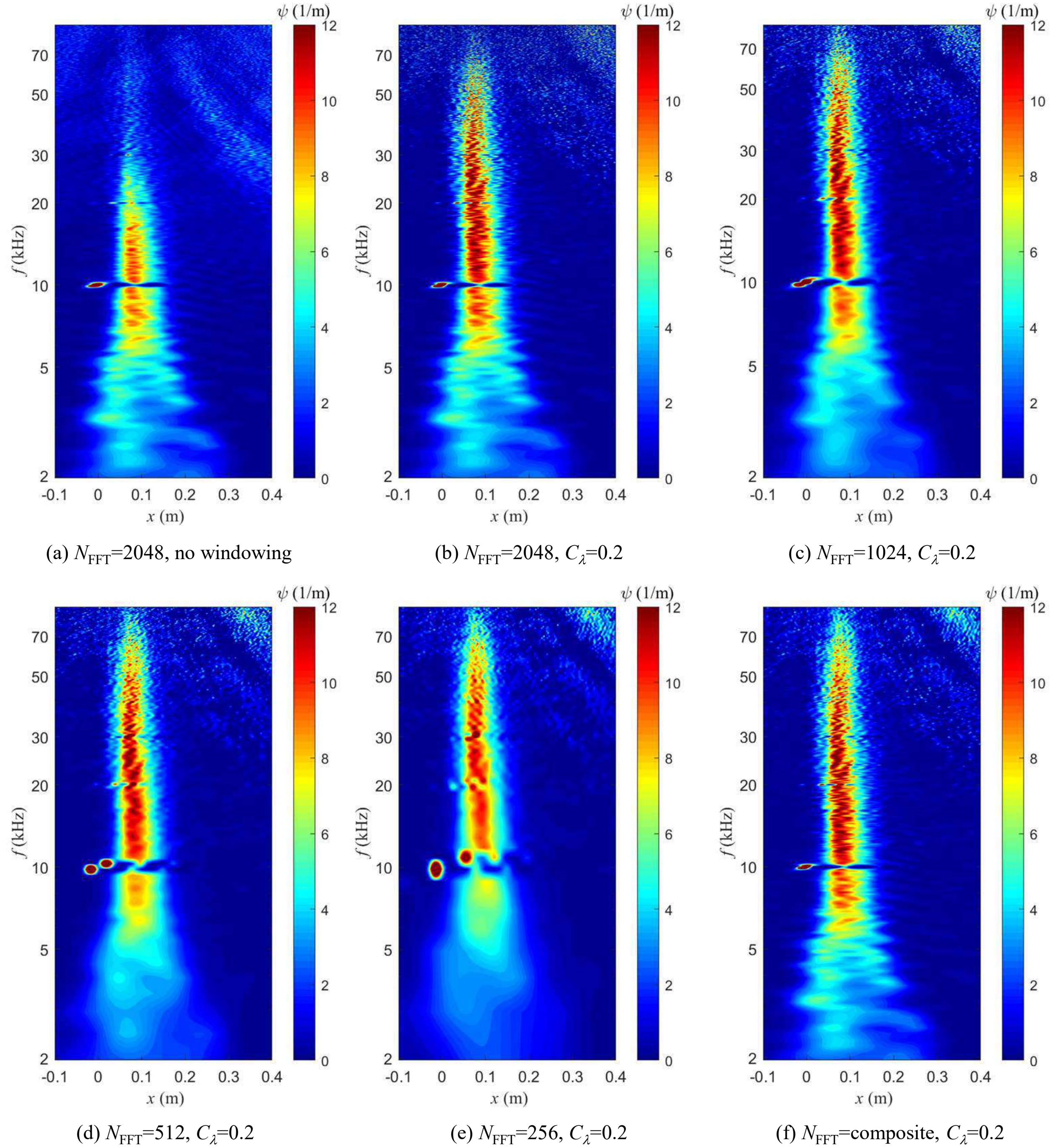

Fig. A3 Effects of frequency-dependent windowing and FFT size on the noise source map of the overexpanded jet. (a) $N_{\mathrm{FFT}} = 2048$**, no windowing; (b)** $N_{\mathrm{FFT}} = 2048$**, windowing with** $c_{\lambda} = 0.2$**; (c)** $N_{\mathrm{FFT}} = 1024$, $c_{\lambda} = 0.2$**; (d)** $N_{\mathrm{FFT}} = 512$, $c_{\lambda} = 0.2$**; (e)** $N_{\mathrm{FFT}} = 256$, $c_{\lambda} = 0.2$**; (f) solution patched from distributions computed with** N_{FFT} **= 2048, 1024, 512, and 256, and** $c_{\lambda} = 0.2$**.**

Appendix B: Bayesian Estimation

This appendix provides background information for the Bayesian estimation approach presented in Section III.C. It distills information found in the seminal papers of Richardson [23] and Lucy [24] and applies it to the direct spectral estimation scheme of this study.

Consider continuously distributed random variables $\widetilde{x}$ and $\widetilde{\xi}$, with x and ξ being specific outcomes, respectively. Denoting the probability by $\mathcal{P}$, probability density functions (pdfs) are defined as follows:

$$
\begin{aligned}
Q(x|\xi)dx \; &= \mathcal{P}\left\{\widetilde{x} \in [x, x+dx] \text{ given } \widetilde{\xi} \in [\xi + d\xi]\right\} \\
P(\xi|x)d\xi \; &= \mathcal{P}\left\{\widetilde{\xi} \in [\xi + d\xi] \text{ given } \widetilde{x} \in [x, x+dx]\right\} \\
\psi(x)dx \; &= \mathcal{P}\left\{\widetilde{x} \in [x, x+dx] \text{ for any } \; \widetilde{\xi}\right\} \\
\phi(\xi)d\xi \; &= \mathcal{P}\left\{\widetilde{\xi} \in [\xi, \xi + d\xi] \text{ for any } \; \widetilde{x}\right\}
\end{aligned}
\tag{B1}
$$

$Q(x|\xi)$ and $P(\xi|x)$ are conditional pdfs; $\phi(\xi)$ and $\psi(x)$ are total pdfs. The pdfs satisfy

$$
\int Q(x|\xi)dx \; = 1 \; ; \int P(\xi|x)d\xi = 1 \; ; \; \int \psi(x)dx = 1; \; \int \phi(\xi)d\xi = 1 \tag{B2}
$$

where $\int$ indicates integration over all the possible outcomes. Requiring that

$$
\mathcal{P}\left\{\widetilde{x} \in [x, x+dx] \text{ and } \widetilde{\xi} \in [\xi + d\xi]\right\} \; = \; \mathcal{P}\left\{\widetilde{\xi} \in [\xi + d\xi] \text{ and } \widetilde{x} \in [x, x+dx]\right\}
$$

we obtain

$$
\phi(\xi)\; Q(x|\xi) \; = \; \psi(x)\; P(\xi|x) \tag{B3}
$$

which is Bayes' theorem for continuous distributions. Integrating over x,

$$
\phi(\xi) \; = \; \int \psi(x)P(\xi|x)dx \tag{B4}
$$

while integrating over ξ,

$$
\psi(x) \; = \; \int \phi(\xi)Q(x|\xi)d\xi \tag{B5}
$$

where the first two equalities of Eq. B2 were used. Equation B4 has the form of Eq. 34 if ξ were thought of as a continuous representation of the discrete "coordinate" $j = 1, \ldots, J$. Equation B5 suggests an inversion of this integral;

however, $Q(x|\xi)$ is unknown. Given prior knowledge of $\psi(x)$, $Q(x|\xi)$ is obtained from Eqs. B3 and B4:

$$Q(x|\xi) \;=\; \frac{P(\xi|x)\psi(x)}{\phi(\xi)} \;=\; \frac{P(\xi|x)\psi(x)}{\int \psi(x)P(\xi|x)dx} \tag{B6}$$

This motivates the construction of an iterative scheme where $\psi(x)$ is estimated from a prior (or initial) distribution. Denoting l the iteration step, Eqs. B5 and B6 are combined into the iterative scheme

$$\psi^{(l+1)}(x) \;= \psi^{(l)}(x) \int \frac{\phi(\xi)P(\xi|x)d\xi}{\int \psi^{(l)}(x)P(\xi|x)dx} \tag{B7}$$

This is the basic Richardson-Lucy deconvolution algorithm.

Looking at Eq. B4 as a general representation of a convolution integral, and setting aside the interpretation of the terms involved as pdfs, in practice these terms may not satisfy the equalities of Eq. B2. In fact, in developing Eq. B7, only the first two equalities were used. The first one, $\int Q(x|\xi)dx = 1$, is user-defined and thus not a limitation. The second one, $\int P(\xi|x)d\xi = 1$, can be relaxed in which case Eq. B5 takes the form

$$\psi(x) \int P(\xi|x)d\xi = \int \phi(\xi)Q(x|\xi)d\xi \tag{B8}$$

and Eq. B7 is generalized to

$$\psi^{(k+1)}(x) \;=\; \frac{\psi^{(k)}(x)}{\int P(\xi|x)d\xi} \int \frac{\phi(\xi)P(\xi|x)}{\displaystyle\int \psi^{(k)}(x)P(\xi|x)dx} d\xi \tag{B9}$$

Performing the discretizations

$$\begin{aligned} \psi(x) \rightarrow &\quad \psi_i \\ \phi(\xi) \rightarrow &\quad \phi_j \\ P(\xi|x)dx \rightarrow &\quad P_{ji} \\ d\xi/dx \rightarrow &\quad c_{ji} \end{aligned} \tag{B10}$$

the convolution integral of Eq. B4 assumes the form

$$\phi_j \;=\; \sum_{i=1}^{N} \psi_i \, P_{ji} \, c_{ji} \tag{B11}$$

and the deconvolution algorithm of Eq. B9 becomes

$$\psi_i^{(l+1)} \;=\; \frac{\psi_i^{(l)}}{\sum_{j=1}^{J} P_{ji} \, c_{ji}} \sum_{j=1}^{J} \frac{\phi_j P_{ji} \, c_{ji}}{\sum_{i=1}^{N} \psi_i^{(l)} P_{ji}} \tag{B12}$$

The term c_{ji} allows for an arbitrary relation between x and ξ, special forms of which may facilitate the inversion. In this study, c_{ji} was set to a constant and thus dropped out of Eq. B12.

Acknowledgment

This work was conducted with NASA Phase I and Phase II SBIR funding, contracts NNX16CC79P and NNX17CC18C, under technical monitor Dr. David Stephens. Partial support for D.M. came from a Balsells Fellowship. The authors acknowledge the contributions of UCI undergraduate students Allan Shtofenmakher, Zihao Zou, and Yunliang Sha to the design and integration of the traverse system. Discussions with Mr. Gary Podboy, NASA Glenn Research Center, on the effect of lip thickness on screech noise have been highly appreciated.

References

[1] Lee, M., and Bolton, J., "Source Characterization of a Subsonic Jet by Using Near-field Acoustical Holography," *Journal of the Acoustical Society of America*, Vol. 121, No. 2, 2007, pp. 967–977. doi:10.1121/1.2404626.

[2] Vold, H., Shah, P., Davis, J., Bremner, P., and McKinely, R., "High-Resolution Continuous Scan Acoustical Holography Applied to High-Speed Jet Noise," *AIAA Paper 2010-3754*, 2010. doi:10.2514/6.2010-3754.

[3] Shah, P., Vold, H., and Yang, M., "Reconstruction of Far-Field Noise Using Multireference Acoustical Holography Measurements of High-Speed Jets," *AIAA Paper 2011-2772*, 2011. doi:10.2514/6.2011-2772.

[4] Stephens, D., and Vold, H., "Order Tracking Signal Processing for Open Rotor Acoustics," *Journal of Sound and Vibration*, Vol. 333, 2014, pp. 3818—-3830. doi:10.1016/j.jsv.2014.04.005.

[5] Comesaña, D., Holland, K., Escribano, D., and de Bree, H.-E., "An Introduction to Virtual Phased Arrays for Beamforming Applications," *Archives of Acoustics*, Vol. 39, No. 1, 2014, pp. 81–88. doi:10.2478/aoa-2014-0009.

[6] Camier, C., Blais, J.-F., Lapointe, R., and Berry, A., "A Time Domain Analysis of 3D Non-Uniform Moving Acoustics Sources: Application to Source Identification and Absolute Quantification via Beamforming," *BeBeC-2012-30*, 2012.

[7] Nicolas, F., "S1MA Wind Tunnel New Aeroacoustic Capability: a Traversing Microphone Array," *AIAA Paper 2018-3137*, 2018. doi:10.2514/6.2018-3137.

[8] Shah, P., Vold, H., Hensley, D., Envia, E., and Stephens, D., "A High-Resolution Continuous-Scan Acoustic Measurement Method for Turbofan Engine Applications," *Journal of Turbomachinery*, Vol. 137, 2015, pp. 121002–121002–11. doi: 10.1115/1.4031341.

[9] Billingsley, J., and Kinns, R., "The Acoustic Telescope," *Journal of Sound and Vibration*, Vol. 48, 1976, pp. 485–510. doi:10.1016/0022-460X(76)90552-6.

[10] Venkatesh, S., Polak, D., and Narayanan, S., "Beamforming Algorithm for Distributed Source Localization and its Application to Jet Noise," *AIAA Journal*, Vol. 41, No. 12, 2003, pp. 1238–1246. doi:10.2514/2.2092.

[11] Brooks, T., and Humphreys, W., “A Deconvolution Approach for the Mapping of Acoustic Sources (DAMAS) Determined from Phased Microphone Arrays,” *Journal of Sound and Vibration*, Vol. 294, 2006, p. 856–879. doi:10.1016/j.jsv.2005.12.046.

[12] Dougherty, R. P., “Extensions of DAMAS and Benefits and Limitations of Deconvolution in Beamforming,” *AIAA Paper 2005-2961*, 2005. doi:10.2514/6.2005-2961.

[13] Sijtsma, P., “CLEAN Based on Spatial Source Coherence,” *International Journal of Aeroacoustics*, Vol. 6, No. 4, 2007, pp. 357–374. doi:10.1260/147547207783359459.

[14] Papamoschou, D., “Imaging of Distributed Directional Noise Sources,” *Journal of Sound and Vibration*, Vol. 330, No. 10, 2011, pp. 2265–2280. doi:10.1016/j.jsv.2010.11.025.

[15] Blacodon, D., and Elias, G., “Level Estimation of Extended Acoustic Sources Using a Parametric Method,” *Journal of Aircraft*, Vol. 41, No. 6, 2004, pp. 1360–1369. doi:10.2514/1.3053.

[16] Papamoschou, D., “Wavepacket Modeling of the Jet Noise Source,” *International Journal of Aeroacoustics*, Vol. 17, No. 1-2, 2018, pp. 52–69. doi:10.1177/1475472X17743653.

[17] Shah, P., Whilte, A., Hendley, D., Papamoschou, D., and Vold, H., “Continuous-Scan Phased Array Measurement Methods for Turbofan Engine Acoustic Testing,” *Journal of Engineering for Gas Turbines and Power*, Vol. 141, No. 8, 2019, pp. 081201–081201–13. doi:10.1115/1.4042395.

[18] Martin, W., and Flandrin, P., “Wigner-Ville Spectral Analysis of Nonstationary Processes,” *IEEE Transactions on Acoustics, Speech and Signal Processing*, Vol. ASSP-33, No. 6, 1985, pp. 1461–1469. doi:10.1109/TASSP.1985.1164760.

[19] White, L., and Boashash, B., “Cross Spectral Analysis of Nonstationary Processes,” *IEEE Transactions on Information Theory*, Vol. 36, No. 4, 1990, pp. 830–835. doi:10.1109/18.53742.

[20] Stockwell, R. G., Mansinha, L., and Lowe, R. P., “Localization of the Complex Spectrum: The S Transform,” *IEEE Transactions on Signal Processing*, Vol. 44, No. 4, 1996, pp. 998–1001. doi:10.1109/78.492555.

[21] Assous, S., and Boashash, B., “Evaluation of the Modified S-Transform for the Time-Frequency Synchrony Analysis and Source Localization,” *EURASIP Journal on Advaces in Signal Processing*, Vol. 49, 2012, pp. 1–18. doi:10.1186/1687-6180-2012-49.

[22] Shanno, D. F., and Phua, K. H., “Minimization of Unconstrained Multivariate Functions,” *ACM Transactions on Mathematical Software*, Vol. 6, No. 4, 1976, pp. 618–622. doi:10.1145/355666.355673.

[23] Richardson, W., “Bayesian-Based Iterative Method of Image Restoration,” *Journal of the Optical Society of America*, Vol. 62, No. 1, 1972, pp. 1–24. doi:10.1364/JOSA.62.000055.

[24] Lucy, L., “An Iterative Technique for the Rectification of Observed Distributions,” *The Astronomical Journal*, Vol. 79, No. 6, 1974, pp. 745–754. doi:10.1086/111605.

[25] Ehrenfried, K., and Koop, L., "Comparison of Iterative Deconvolution Algorithms for the Mapping of Acoustics Sources," *AIAA Journal*, Vol. 45, No. 7, 2007, pp. 1584–1595. doi:10.2514/1.26320.

[26] Antoni, J., "A Bayesian Approach to Sound Source Reconstruction: Optimal Basis, Regularization, and Focusing," *Journal of the Acoustical Society of America,*, Vol. 131, No. 4, 2012, pp. 2873–2890. doi:10.1121/1.3685484.

[27] Pereira, A., Leclère, Q., and Antoni, J., "Empirical Bayesian Regularization of the Inverse Acoustic roblem," *Applied Acoustics*, Vol. 97, 2015, pp. 11–29. doi:10.1016/j.apacoust.2015.03.008.

[28] Leclère, Q., Pereira, A., Bailly, C., Antoni, J., and Picard, C., "A Unified Formalism for Acoustic Imaging Based on Microphone Array Measurements," *International Journal of Aeroacoustics*, Vol. 16, No. 4-5, 2017, pp. 431–456. doi:10.1177/1475472X17718883.

[29] Gerhold, C., Clark, L., Dunn, M., and Tweed, J., "Investigation of Acoustical Shielding by a Wedge-Shaped Airframe," *Journal of Sound and Vibration*, Vol. 294, No. 1-2, 2006, pp. 49–63. doi:10.1016/j.jsv.2005.10.010.

[30] Raman, G., "Advances in Understanding Supersonic Screech: Review and Perspective," *Progress in Aerospace Sciences*, Vol. 34, 1998, pp. 45–106. doi:10.1016/S0376-0421(98)00002-5.

[31] Tam, C., Parrish, S., and Viswanathan, K., "Harmonics of Jet Screech Tones," *AIAA Journal*, Vol. 52, No. 11, 2014, pp. 2471–2478. doi:10.2514/1.J052850.

[32] Liu, J., Corrigan, A., Kailasanath, K., Heeb, N., and Gutmark, E., "Numerical Study of Noise Characteristics in Overexpanded Jet Flows," *AIAA Paper 2015-0508*, 2015. doi:10.2514/6.2015-0508.

[33] Dougherty, R., and Podboy, G., "Improved Phased Array Modeling of a Model Jet," *AIAA Paper 2009-3186*, 2009. doi:10.2514/6.2009-3186.

[34] Laasmaa, M., Vendelin, M., and Peterson, P., "Application of Regularized Richardson-Lucy Algorithm for Deconvolution of Confocal Microscopy Images," *Journal of Microscopy*, Vol. 243, No. 2, 2011, pp. 124–140. doi:10.1111/j.1365-2818.2011.03486.x.

[35] Karjalainen, M., and Paatero, T., "Frequency-Dependent Signal Windowing," *IEEE Workshop on Applications of Signal Processing to Audio and Acoustics*, 2001. doi:10.1109/ASPAA.2001.969536.